



Cite this: *Nanoscale*, 2022, **14**, 11098

Atomic force microscopy probing interactions and microstructures of ionic liquids at solid surfaces

Rong An, ^aAatto Laaksonen, ^{b,c,d,e}Muqiu Wu, ^aYudan Zhu, ^eFaiz Ullah Shah, ^fXiaohua Lu^e and Xiaoyan Ji^{*b}

Ionic liquids (ILs) are room temperature molten salts that possess preeminent physicochemical properties and have shown great potential in many applications. However, the use of ILs in surface-dependent processes, e.g. energy storage, is hindered by the lack of a systematic understanding of the IL interfacial microstructure. ILs on the solid surface display rich ordering, arising from coulombic, van der Waals, solvophobic interactions, etc., all giving near-surface ILs distinct microstructures. Therefore, it is highly important to clarify the interactions of ILs with solid surfaces at the nanoscale to understand the microstructure and mechanism, providing quantitative structure–property relationships. Atomic force microscopy (AFM) opens a surface-sensitive way to probe the interaction force of ILs with solid surfaces in the layers from sub-nanometers to micrometers. Herein, this review showcases the recent progress of AFM in probing interactions and microstructures of ILs at solid interfaces, and the influence of IL characteristics, surface properties and external stimuli is thereafter discussed. Finally, a summary and perspectives are established, in which, the necessities of the quantification of IL–solid interactions at the molecular level, the development of *in situ* techniques closely coupled with AFM for probing IL–solid interfaces, and the combination of experiments and simulations are argued.

Received 21st May 2022,
Accepted 14th July 2022

DOI: 10.1039/d2nr02812c
rsc.li/nanoscale

1. Introduction

Ionic liquids (ILs) are molten salts, composed mainly of organic cations and inorganic anions, with melting points below 100 °C. They show many exceptionally attractive properties, such as nonflammability, excellent thermal stability, negligible vapor pressure, intrinsic ionic conductivity, molecular designability and a wide electrochemical voltage window.^{1–5} These and other unique properties make ILs highly promising in various fields, such as lubrication,^{6,7} energy storage,^{8–15} gas separation,^{16–18} and green catalysis,^{19,20} to mention a few.

In many applications, ILs are often in direct contact with a solid surface.^{5,21} The interface drastically alters their microstructure and dynamics,²² making the ILs near to the surface

significantly different from those in bulk.^{5,21,23–25} For example, a shift from a liquid to solid phase has been observed for the ILs adjacent to solid surfaces, which becomes even more pronounced on metallic surfaces.²⁶ For the dynamics, a slower diffusion was observed in the ILs confined between graphite walls than that in bulk,²⁷ while a significantly increased ion diffusion has been observed in some other types of confined systems both experimentally and theoretically.^{28–31} For example, the diffusion coefficient of ions in the phosphonium bis(salicylato)borate IL confined in 4 nm Vycor pores was found to be 35–40 times higher than that in bulk.³⁰

Both the dynamic behavior and microstructure of ILs on solid interfaces depend on the surface properties, such as roughness, chemistry, and charges, together with the molecular structures of ILs themselves, but also on the external conditions, such as temperature, pressure, and electric field.^{32–37} The ILs on the solid surface can display rich ordering,^{38–44} arising from both long-range coulombic and short-range van der Waals interactions, hydrogen bonding, dipole–dipole and various solvophobic interactions,³³ all giving the near-surface ILs distinct microstructures. For example, an ordered crystalline phase of ILs coexists with a mobile liquid phase on a graphite surface, caused by comparable strengths between IL–surface and IL–IL interactions;⁴⁵ extended layering structures of ILs on solid surfaces were observed in the AFM force–distance profiles, as a consequence of both the adjacent IL–solid

^aHerbert Gleiter Institute of Nanoscience, School of Materials Science and Engineering, Nanjing University of Science and Technology, Nanjing 210094, China. E-mail: ran@njust.edu.cn

^bEnergy Engineering, Division of Energy Science, Luleå University of Technology, 97187 Luleå, Sweden. E-mail: xiaoyan.ji@ltu.se

^cDepartment of Materials and Environmental Chemistry, Arrhenius Laboratory, Stockholm University, SE-10691 Stockholm, Sweden

^dCenter of Advanced Research in Bionanocartridges and Biopolymers, "Petru Poni" Institute of Macromolecular Chemistry, Iasi 700469, Romania

^eState Key Laboratory of Materials-Oriented and Chemical Engineering, Nanjing Tech University, Nanjing 211816, China

^fChemistry of Interfaces, Luleå University of Technology, 97187 Luleå, Sweden

and bulk IL-IL interaction strength,^{22,41} and a similar extended layering of packed IL ions on mica surfaces is observed, which resulted from an ion exchange between K⁺ and the IL cations on the mica surface.⁴⁶

All these observed microstructures for the interfacial ILs, due to the variation of IL-solid interactions, are highly important in phenomena like capacitance and nanoscale friction.^{21,47,48} A surface-active IL electrolyte, containing amphiphilic structures, can exhibit an atypical bilayer ion packing, which is different from conventional alternating layers. This is because the strong van der Waals interactions enhance the charge storage performance.⁸ Nevertheless, more structured ion layers at a gold electrode were reported under higher cathodic electrode potentials to slow down the capacitive process.⁴⁹ The ordered IL layers that are formed at interfaces can result in both higher^{50–52} and smaller^{51,53,54} nanoscale friction. The higher friction is attributed to a greater ion excess concentration in the more ordered layer, causing a stronger attractive interlayer interaction within the same contact area.⁵⁰ An opposite effect of an ordered IL layer on the friction can be ascribed to the plane of smoothly packed ions, which is beneficial for friction reduction.

Therefore, a good understanding and control of the chosen ILs, their interactions with the solid interfaces, and how they are affected by the external conditions are needed to create assemblies for applications like super-lubrication systems and high-performance energy storage devices. Still, the specific role and relative importance of these interactions in determining the structure and properties of ILs are not well understood, hindering a more widespread application of ILs in many technological applications.⁵⁵ Furthermore, a large number of IL cations and anions are now available, and in applications,

many of them need to be easily mixed with each other or with other organic and inorganic polar solvents, giving a practically infinite number of systems with tunable properties. Using solid interfaces with a wide variety of adjustable properties further imposes challenges in identifying an optimum IL for any given solid surface in any specific application. Therefore, it is highly important to analyze and clarify the interactions of ILs with solid interfaces at the nanoscale to understand the microscopic structure and mechanisms, providing us with quantitative structure–property relationships.

The appearance of atomic force microscopy (AFM) did open a surface-sensitive way to directly probe the interaction strength of ILs with solid surfaces in the layers from sub-nanometers to micrometers. AFM can probe IL-solid interfaces at the nanoscale and has far-reaching implications in many areas of science. AFM allows obtaining the microstructure, *i.e.*, the ion layering and composition of ILs at solid surfaces as well as the interaction force between the surface and adjacent IL molecules which cannot be explained by continuum theories of van der Waals, or electrostatic interactions.⁴¹ Many excellent reviews discuss the unique possibilities offered by AFM to study IL-solid interfaces.^{5,6,21,41,56–58} However, so far, (i) they mainly focus on the distinct behavior of ILs at solid interfaces, (ii) they mainly report advances in IL-based applications, such as lubrication and electrolytes, (iii) they only partially highlight recent research on interfacial IL microstructures and then as a consequence of longitudinal IL-solid interactions, and (iv) they pay less attention in using AFM to probe the local structure and properties of the near-surface ILs. With the annual number of publications of ILs, these reviews tend to become outdated rapidly. Therefore, we provide here an AFM-based comprehensive roadmap of ion microstructures across longi-



Rong An

Dr Rong An received her Ph.D. in Chemical Engineering from Nanjing Tech University, China, in 2013. She then worked as a postdoc researcher in Chemical and Biomolecular Engineering at North Carolina State University from 2013 to 2015. She joined the School of Materials Science and Engineering/Herbert Gleiter Institute of Nanoscience, at Nanjing University of Science and Technology in 2015. Her current position is Associate Professor. Her research interests include ionic liquid–solid interactions, interface and surface science, liquid–solid interfacial phenomena, ionic liquid-based lubrication, gas separation, etc.

Published on 14 July 2022. Downloaded on 2/24/2025 3:56:22 AM.



Aatto Laaksonen

Dr Aatto Laaksonen is a Professor of Physical Chemistry at Stockholm University (SU). He received his Ph.D. in 1981 (SU), and was a PDF at Daresbury Laboratory (U.K.) in 1982 with Vic Saunders and at IBM Poughkeepsie/Kingston (U.S.A.) from 1983 to 1985 with Enrico Clementi. He was on sabbatical at Dalhousie University (Canada) in 1993–1995 with Rod Wasylissen. He was a visiting professor at JAERI (Japan) in 2002 and 2005, at Cagliari University (Italy) in 2008, 2009, 2011, and 2015, at Nanjing Tech University (China) from 2018–present, Petru Poni Institute (Romania) from 2018–present and Luleå University of Technology from 2020–present. His current research focuses on multiscale modelling/simulations, method/model development in bio and materials sciences and green chemical engineering with 250+ journal articles.

tudinal and lateral directions, regarding the interactions of ILs with solid surfaces, as a function of surface properties, IL characteristics, and external stimuli.

The very aim of this review is to go deep into the origin of interactions and microstructures of ILs on solid interfaces through the AFM probe to determine their delicate interplay, allowing a molecular understanding in the design of specific near-surface properties of ILs to further help achieve the control of interfacial IL behavior. This review starts with a brief introduction of AFM for probing the interaction forces of ILs at solid interfaces, which can be characterized by adhesion force, friction coefficient, and slip length, with correlations to the microstructures of interfacial ILs (section 2). The influence of the characteristics of ILs and the combined surface properties on the modes of interactions and microstructure of the interfacial ILs are thereafter discussed in section 3 and section 4, respectively, followed by the effects of external stimuli in section 5. Prospects for future research directions are proposed, and conclusions are drawn at the end of this review (section 6). In conclusion, we argue the necessity for the quantification of IL–solid interactions at the molecular level, the development of *in situ* techniques closely coupled with AFM for probing IL–solid interfaces, and the close combination of experiments and simulations.

2. Atomic force microscopy on ionic liquid–solid interfaces

In 1986, atomic force microscopy (AFM) was invented to contour surfaces with atomic resolution, which was an important milestone in the history of nanoscience and nanotechnology.^{59–63} The arrival of ‘daughter’ instruments of AFM, such as the lateral force microscopy, enabled simul-



Faiz Ullah Shah

Dr Faiz Ullah Shah is an Associate Professor in Chemistry of Interfaces at Luleå University of Technology, Sweden. He received his Ph.D in 2011 in Chemistry of Interfaces from Luleå University of Technology, Sweden. He joined the Chemistry of Interfaces research group at Luleå University of Technology as an Associate Senior Lecturer in 2013. His research areas cover synthesis and characterization of fluorine-free functional ionic

liquids for a range of applications, e.g., batteries and supercapacitors, lubrication, and gas separation.

taneous morphological and mechanical characterization, as well as the manipulations of atoms, molecules, and clusters, was observed. During the detection with an AFM technique, a probe at the end of a cantilever is brought into the close vicinity of the surface and scanned over the sample with piezoelectric scanners (Fig. 1a).⁶⁴

Conventionally, AFM is used to detect the topographic images of both conducting and insulating surfaces, by plotting the deflection of the cantilever *versus* its position on the sample. The AFM imaging contrast arises from the probe–sample interactions, which depends not only on the probe–sample separation but also the material properties of both the probe and the sample, and any of them could be used as a feedback parameter to track the surface topography.^{65,66}

Notably, the state-of-the-art AFM techniques⁶¹ have provided a highly sensitive measure of interactions and microstructural mapping at interfaces. In the area related to ILs, the work can be briefly classified into three fields. Firstly, the force–distance curve measurement by AFM (section 2.1) has been used to detect the interaction force of ILs with solid surfaces. As the ion layer is resistive against an external pressing force to a certain extent, the layering structure of ILs, the number and thickness of these layers, as well as the force that each layer can resist can be obtained.⁶⁷ Secondly, AFM has been used to establish the relationships between IL interfacial structures and nanoscale friction^{51,68} (section 2.2). Thirdly, the AFM colloid probe has been utilized as a nanotool to obtain the slip length of ILs at solid interfaces, describing the dynamics and microstructures of near-surface ILs (section 2.3).^{69–75} A schematic operation is shown in Fig. 1(b).

2.1. Force–distance curves

In an AFM experiment, the deflection of the cantilever and the vertical position of the probe are recorded, which is known as



Xiaohua Lu

Dr Xiaohua Lu is a Professor of Chemical Engineering at Nanjing Tech University. He received his PhD in Chemical Engineering from Nanjing University of Chemical Technology in 1988. He has been a leader in fundamental theoretical modelling and experimental measurements for complex fluids with interfaces. In particular, he proposed and developed the concept of the “ion hydration factor” for ionic solutions, which enabled the

development of the Lu–Maurer model to calculate chemical potential gradients for nonideal, non-equilibrium complex fluids. He also pioneered the extension of non-equilibrium statistical mechanics to interfaces. To date, he has published 300+ journal articles.

the “force–distance curve” and briefly called “force curves”. Such detection enables the investigation of the properties of the detected sample, the used probe, or the chosen medium in between. The adhesion force is measured with the force curves method, where the AFM probe is first brought into contact with the sample surface; when retracting the probe from the sample surface, the force required to separate the probe from the sample surface is called a pull-off or adhesion force.^{69–75} A previous finding obtained quantitative interaction forces between metals and graphene by AFM force curves, in which the probes are coated with various metals by vacuum evaporation allowing a direct measurement of the metal–graphene forces.⁷⁶

To further illustrate the force curve detection, an IL-coated highly ordered pyrolytic graphite (HOPG) surface with an AFM probe was chosen as the example.⁵² A typical force curve is presented in Fig. 1(b). In general, when the probe moves towards the IL-film, it cannot interact with the IL film (A) at a long distance, and a sudden jump in the force is observed at a defined position (B) caused by the capillary force. After the jump, the probe remains at a certain distance (C) away from the HOPG substrate, *i.e.*, it is not in contact with HOPG; upon further approach, a steep linear increase in the force is observed (D), indicating the contact with HOPG. As the probe is retracted (E), it will be separated from the surface once the force exceeds the contact adhesion force. Afterward, a gradually decreasing attractive force is observed between the probe and the IL film (F, G). The zero-force line is reached again (H) when the probe is completely released from the IL film.

The force curves obtained in AFM can be divided into short- and long-range regions. For the IL-related systems, the solvation force (<10 molecular diameters) is of typical short-range origin.⁷⁷ Due to the relatively strong liquid–solid interaction, the molecular structure of ILs close to the solid interface is significantly different from that in the bulk phase, and their density profile oscillates periodically (Fig. 2). This induced liquid ordering is termed the “solvation layer”, extending a few molecular diameters from the interface. The

formation of discrete solvation layers results in exponentially decaying oscillatory force, which is also called as “solvation force”.^{41,66}

The long-range force normally comprises the attractive van der Waals force ($\sim 10^{-8}$ m) and electrostatic force ($\sim 10^{-7}$ m). The presence and magnitude of long-range force in ILs are significantly influenced by surface properties, and a pronounced long-range force has only been observed in ILs when they are located at charged surfaces. While surface properties have little impact on the decay length of the long-range interaction force, significant differences are observed in that of short-range forces.²² The long-range van der Waals force arises mainly from the fluctuations in the electric dipole moments of molecules.^{79–82} The sphere-flat geometry is the most common approximation to describe the van der Waals force, which is proportional to $1/r^6$ with r as the instantaneous distance between the interacting atoms or molecules.⁸³ The long-range electrostatic forces come basically from the effect of electric fields on electrical charges.⁸² In most IL-surface force studies, however, such specific electrostatic forces cannot be observed.⁸⁴ This can be explained as follows: the electrostatic force drives the formation of ionic (polar) domains in ILs, from which the alkyl chains (nonpolar) are solvophobically excluded and thus cluster into nonpolar domains.⁸⁵ ILs are typically composed of large, asymmetric polyatomic ions, which sterically increase the separation and enlarge the distance between cation and anion charge centers, weakening the electrostatic interactions. The interionic electrostatic interactions of ILs can also be weakened by the presence of water especially in the atmosphere, effectively screening the ion–ion correlations.^{86,87} Rarely, the electrostatic force in ILs can be observed under other controlled conditions *via* AFM or Surface Force Apparatus.^{34,84,88–90} For example, a sharp transition from the complete screening of electrostatic forces to apparently Debye like behavior occurred in the IL ethylammonium nitrate (EAN) when the temperature was elevated from 373 to 373 and 393 K, exhibiting a significant temperature dependence;^{22,84,90} pronounced electrostatic forces were observed in the EAN confined between or locally directly being adjacent to charged surfaces.^{34,84,88–91}

Besides, when the surfaces are covered by a thin IL film or the studied IL condenses between the AFM probe and sample, a long-range attractive capillary force ($\sim 10^{-9}$ – 10^{-3} m) will be present. In a typical AFM force curve of a thin IL film on HOPG with AFM glass colloidal probes (Fig. 1b), the probe first contacts the IL surface during the approach, and a meniscus is formed. The attractive force gradually increases on a continued approach until the probe reaches the HOPG substrate, whereafter ionic repulsion forces take over. The attractive force observed in this presented approach curve includes not only the capillary force but also the van der Waals and electrostatic forces. When retracting the probe, a pull-off force of 977 nN is needed to break the meniscus. The capillary force has drastic effects on the contrast mechanism of AFM contact imaging, and it might cause plastic deformation on soft samples. Consequently, the capillary force needs to be avoided



Xiaoyan Ji

Dr Xiaoyan Ji is a full Professor in the Division of Energy Science at Luleå University of Technology, Sweden. She received her Ph.D. in Chemical Engineering from Nanjing Tech University, China, in 2000 and has 20+ years of experience in research and development in the area of Chemical Engineering and Energy Engineering. Her research work spans from theoretical modeling to technology development, process simulation and integration. To date, as a first author or main contributor, she has published 150+ journal articles.

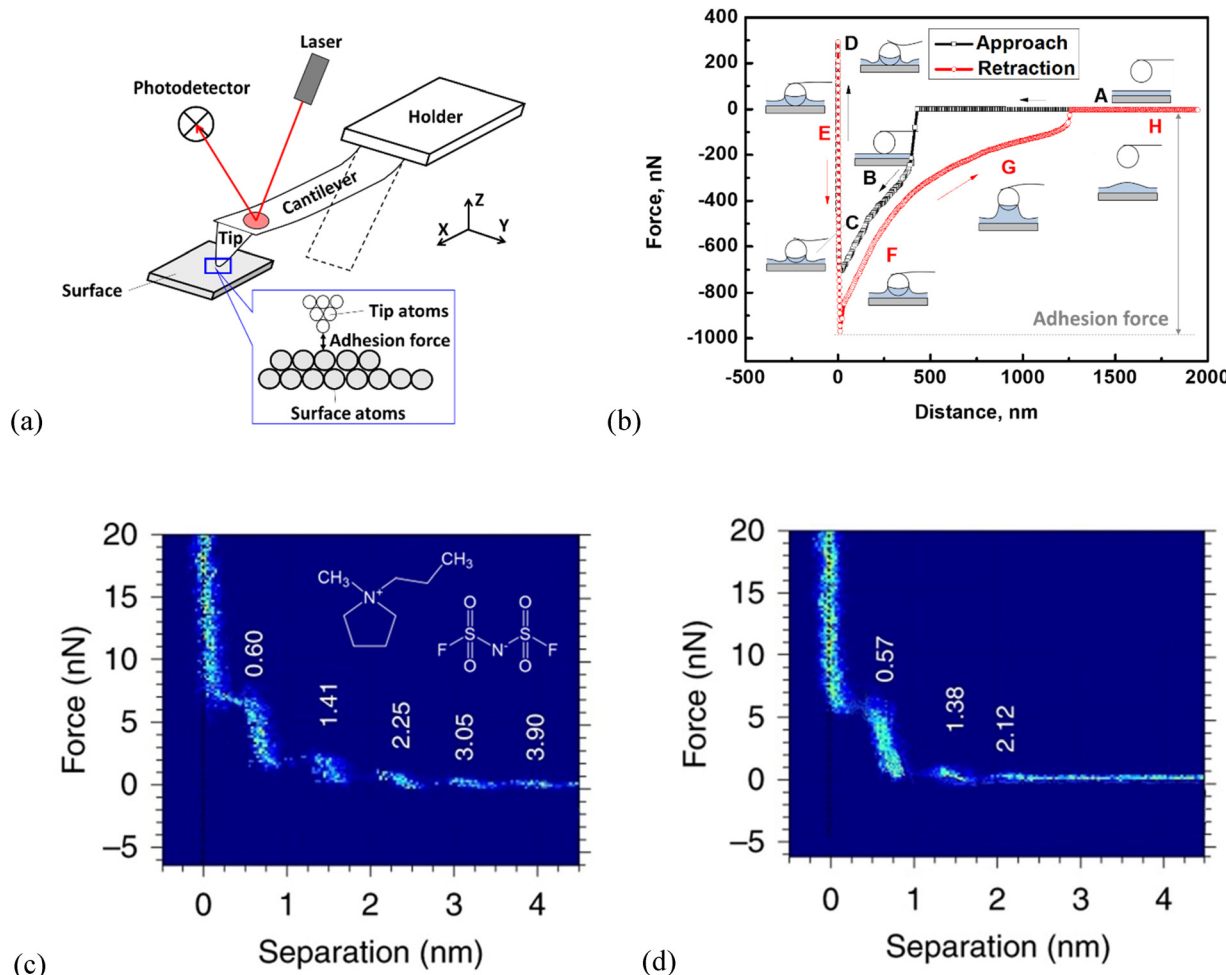


Fig. 1 (a) Schematic presentation of the working principle in atomic force microscopy (AFM). (b) Typical force vs. distance curves measured using an AFM glass colloidal probe on an IL-coated highly ordered pyrolytic graphite (HOPG) substrate. The IL is $[\text{BMIM}]\text{[PF}_6]$ (1-butyl-3-methylimidazolium hexafluorophosphate). The inset scheme for the colloidal probe at the end of a cantilever approaching the IL film on a HOPG support (A–D) is retracted after contact (E–H). Force–distance curves of the IL $[\text{C}_3\text{mpyr}]\text{[FSI]}$ with different NaFSI salt concentrations of (c) 0 mol%, (d) 50 mol% on gold electrodes at open circuit potential (OCP).⁹ Copyright 2020, Springer Nature. The inset in (c) is the molecular structure of the IL N -methyl- N -propylpyrrolidinium bis(fluorosulfonyl)imide $[\text{C}_3\text{mpyr}]\text{[FSI]}$.

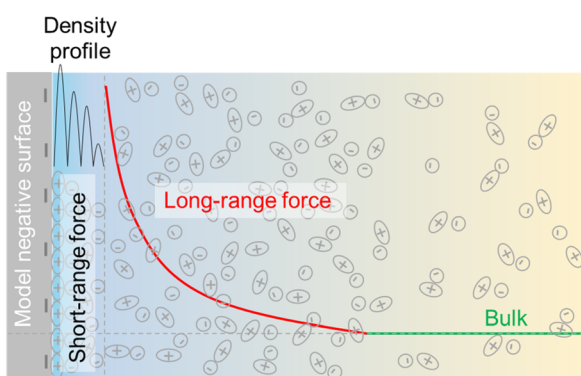


Fig. 2 Schematic illustrating the short- and long-range forces for ILs in contact with a model negatively charged surface.⁷⁸ Copyright 2019, Elsevier.

in AFM imaging. One way to circumvent the presence of capillary forces is to immerse the probe and sample into liquid, while the other strategy is to incorporate the instrument in a vacuum or dry nitrogen environment,⁹² or the employment of small-size AFM probes.⁹³

AFM force–distance curves can also provide a direct insight into the microstructure of ions at the IL-solid interfaces. Nowadays, AFM is often used to study the periodicity of the solvation structure in ILs at solid substrates. The characteristic oscillation length of AFM force curves corresponds to the diameter of the IL ions when the substrate or the AFM probe is uncharged, but it is related to the ion-pair diameter when both the substrate and the probe are charged.⁹⁴ It is worth noting that the ion structure of ILs is responsive to both liquid and surface effects, different from the solvation layer of conventional molecular liquids. The key difference is that many ILs possess bulk order which can be propagated over much greater distances than conventional molecular liquids, and the ions

form a network of polar and non-polar domains caused by electrostatic and solvophobic clustering.⁴¹ In Fig. 1(c) and (d), the ion layering microstructures of *N*-methyl-*N*-propylpyrrolidinium bis(fluorosulfonyl)imide ($[C_3\text{mpyr}][\text{FSI}]$) IL at gold electrodes as well as the distinct effect of NaFSI salt on it were captured. As shown in Fig. 1(c), five oscillations were measured for $[C_3\text{mpyr}][\text{FSI}]$ before the repulsion became so strong that it prevented a closer approach to the gold surface. The step period of 0.6 nm was consistent with the size of the ion pair, suggesting the cation and anion are present in approximately equal numbers in the layers. The solvation force required to squeeze-out a layer decreased further away from the surface as the ordering of the layered ions was lowered. After adding 50 mol% NaFSI to the IL $[C_3\text{mpyr}][\text{FSI}]$ (Fig. 1d), the ion structure was dramatically changed compared with the neat IL in Fig. 1(c), with fewer steps along with a large decrease in the solvation force. As shown in Fig. 1(d), the rupture solvation force required to break each layer is reduced in the NaFSI salt system due to the weakening of the ion-ion association. The position of the steps is also shifted in the mixture of the IL and NaFSI salt compared with the neat IL, indicating the changed dimensions of ion packing caused by the addition of NaFSI. The disruption of these layered ion structures by NaFSI is attributed to the existing Na^+ at the interface, altering the chemical composition of the inner electrolyte layers.⁹ In addition, the surface charge and roughness as well as the orientation of cations at the interface are critical determinants of the solvation layer in ILs, which can be mapped clearly through the AFM force curves. In particular, highly charged and rough surfaces exhibited negative effects on the formation of solvation layers, and the AFM probe radius only influences the amplitude of the force but not the period.⁴³

To briefly summarize, the short- and long-range forces of near-surface ILs reflected by AFM force curves have been distinguished, and the regimes of the two forces are part of a continuous whole, without any physical boundary in between. The short- and long-range forces drive the formation of different ion structures in ILs at solid interfaces, in which, the short-range structure typically extends to 10 molecular diameters away from surfaces, while the long-range force regime can even extend to 10^{-3} m, depending on the IL–surface combination.²² This highlights the fact that IL properties and surface features are critical determinants of near-surface forces in ILs, which would be discussed systematically in sections 3 and 4.

2.2. Nanoscale friction

The AFM force curves allow us to “monitor” what is going on across the longitudinal direction at the buried IL–solid interfaces. The lateral information of the interfacial ILs can be acquired through the AFM-measured friction force. The investigation of macroscopic frictional phenomena is as old as time, and a pioneering attempt to understand the friction establishment^{95–97} reveals that friction force is linearly proportional to the normal load. However, the friction becomes far more complicated for the ILs with nanoscale films between

two sliding solid contacts, which can be termed nanoscale friction or nanofriction.

The nanoscale friction force can be detected with AFM by scanning the surface of the ILs back and forth under the probe at 90° angle to the cantilever long axis (Fig. 3a). During the detection, the traces of cantilever lateral diffraction (friction loops, cf. inset in Fig. 3a) over a scan area with a sliding velocity are recorded. For each friction loop, the difference in the friction signal (in voltage) between the forward (trace) and reverse (retrace) scans can be converted to friction force (in Newton) by applying Hooke's law.

The detected nanoscale friction force F_F is contributed by load- and adhesion-controlled terms:^{98,99}

$$F_F = \mu F_N + F_0 \quad (1)$$

where F_N is the normal load, and the intercept F_0 is the adhesion-controlled static friction force term at zero sliding velocity and zero normal load.

Following eqn (1), the friction force increases linearly with increasing load, and a typical example is shown in Fig. 3(b), where the silicon nitride AFM probe on a mica deposited by $[\text{BMIM}][\text{PF}_6]$ was focused. A straight line is fitted to the plot using linear regression, and the friction coefficient μ is determined from the slope, and the nonzero intercept with the vertical axis is the adhesion-controlled term. The adhesion arises mainly from the van der Waals, electrostatic, and attractive capillary meniscus forces,¹⁰⁰ which is significant for the molecular liquid system. However, the adhesion is strongly dependent on the studied system, and it can be progressively weakened when adding IL to the molecular liquid (e.g., the oil hexadecane, Fig. 3c). This is because the added IL molecules adsorbed on the solid substrates, preventing the direct probe-substrate contact through steric effects from the IL alkyl chains or electrostatic repulsion, and overcoming the attractive van der Waals forces.¹⁰¹

The AFM-measured nanoscale friction force at IL–solid interfaces can also provide an insight into the ion ordering microstructures of the interfacial ILs. For example, a two-regime nanofriction feature was observed in EAN on mica at room temperature, as shown in Fig. 3(d), where the small loads (<20 nN) correspond to the probe shearing against the more loosely ordered ion layers. While at higher loads (>20 nN) the probe penetrates the near-surface layer and shears against the highly ordered IL on the surface.¹⁰² Based on the results of the friction force *versus* the normal load for 1-pentylopyridinium bis(trifluoromethanesulfonyl) imide ($[C_5\text{Py}][\text{NTf}_2]$) at a mica surface (Fig. 3e) with two friction regimes, the IL microstructure can be abstracted as follows. Multiple layers of ion-pairs separate the AFM probe from the surface in the low load regime, while the probe slides against the boundary layer in the high load regime.¹⁰³ The critical normal load of the transition from the multilayer to boundary regime is ~ 3 nN, in good agreement with the rupture force of ~ 2 nN in the normal force curve (Fig. 3e, inset).¹⁰⁴ In the boundary regime with a normal load of >3 nN the friction

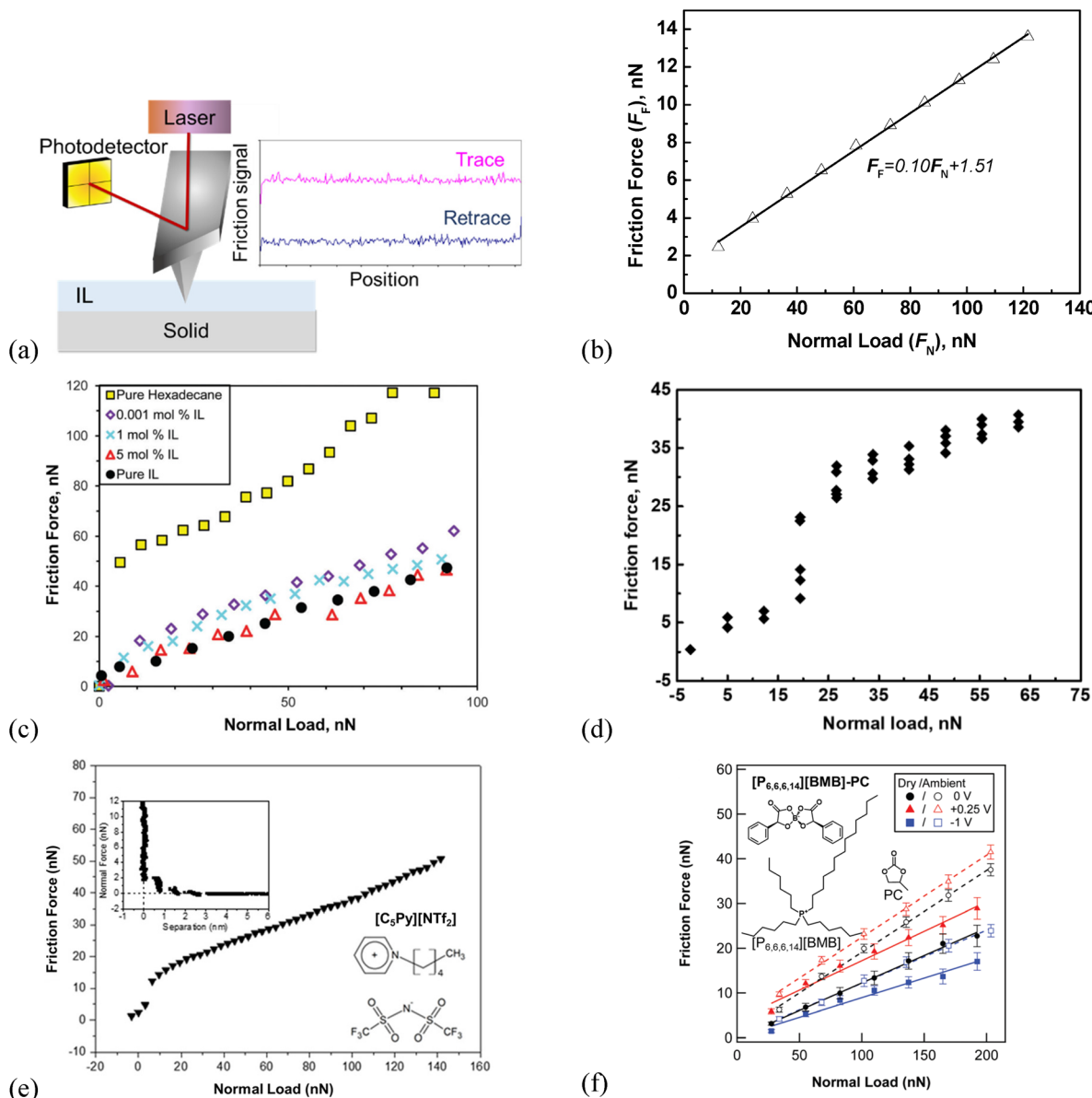


Fig. 3 (a) Schematic diagram of the lateral friction force measurement by AFM and typical friction-loop curves. Friction-load plots obtained by (b) silicon nitride probe (radius ~ 20 nm) on the mica surface deposited by the IL $[BMIM][PF_6]$, (c) sharp silicon probe (radius ~ 8 nm) on Au(111) surfaces deposited by hexadecane- $[P_{6,6,6,14}]^+[(C_8)_2PO_2^-]$ mixtures. $[P_{6,6,6,14}]^+[(C_8)_2PO_2^-]$ = trihexyl(tetradecyl)phosphonium bis(2,4,4-trimethylpentyl)-phosphinate,¹⁰¹ Copyright 2016, Royal Society of Chemistry. (d) Colloid silica probe (radius ~ 3.4 μ m) in EAN supported by mica at room temperature,¹⁰² Copyright 2016, Royal Society of Chemistry. (e) Silicon probe in the IL 1-pentylpyridinium bis(trifluoromethanesulfonyl) imide, $[C_5Py][NTf_2]$ at mica surfaces,¹⁰³ Copyright 2020, American Chemical Society. The inset showing a force-distance curve,¹⁰⁴ Copyright 2019, American Chemical Society. And (f) sharp silicon probe (radius ~ 7 nm) in a solution of 20% w/w $[P_{6,6,6,14}][BMB]$ in PC on a gold electrode surface at three applied potentials (0, -1 and +0.25 V) in dry (Ar) and ambient (relative humidity (R.H.) = 22%) conditions at a velocity of 6 μ m s⁻¹, solid and dashed lines represent the linear fits to obtain friction coefficients, $[P_{6,6,6,14}][BMB]$ = trihexyltetradecylphosphonium bis(mandelato)borate, PC = propylene carbonate.¹⁰⁵ Copyright 2020, Royal Society of Chemistry.

coefficient is relatively small because of the smooth cation enriched boundary layer.

The microstructure depends on the environment (e.g., water and surface potential), which can also be studied via the nanofriction measurements. For example, the friction of trihexyltetradecylphosphonium bis(mandelato)borate ($[P_{6,6,6,14}][BMB]$) and propylene carbonate on electrified gold is higher

in the presence of water (Fig. 3f). This is because the interactions among the IL-ions are weaker in the water environment, and the load-bearing capability of ion layers is reduced. While under a negative potential, a low friction is observed, no matter with water or not,¹⁰⁵ being ascribed to the existence of long alkyl chains in $[P_{6,6,6,14}]^+$. These cation chains facilitate the formation of robust interfacial layers through the van der

Waals force, while they are disrupted at positive potentials by the small and sterically hindered $[\text{BMB}]^-$.¹⁰¹

The frictional phenomena are more complex in soft contact interfaces, such as those composed of liquid/liquid or liquid/solid interfaces, because interfacial structural transitions might occur at high normal loads. For example, a negative friction coefficient was observed on the lamellar graphite surface during the AFM probe retraction process, *i.e.*, the friction force increases as the normal load decreases.¹⁰⁶ It has also been observed in other systems, such as two-dimensional materials^{107–112} and phosphonium-based IL/glycol ether mixtures on titanium substrates with a silicon nitride probe.²⁸ For the ILs, the structural reorientation of the ions is responsible for the negative load dependence, *i.e.*, the cation alkyl chains preferentially stay in parallel to the probe scanning path as the normal load increases, which is favorable in reducing the friction force.²⁸ Furthermore, the nonlinear variation of friction with a normal load (non-Amontons' behavior) was found for a silicon AFM probe sliding on the surface of a silicon (100) wafer under 1-ethyl-3-methylimidazolium bis(trifluoromethylsulfonyl)imide ($[\text{EMIM}][\text{TFSI}]$), which cannot follow the assumption of the friction-contact area proportionality projected by continuum-contact-mechanics models.¹¹³

Neither negative nor nonlinear correlation between the friction force and the normal load is inherent in Amontons' law. To achieve a quantitative description of the complex nanoscale frictional phenomena at IL-solid interfaces, some information about the origin of friction coefficients can be derived as follows. Based on the assumption^{95,114} that there exists a situation where an IL is being sheared in the x -direction between two solid surfaces, the friction coefficient μ is closely related to the IL viscosity, η (Pa s), sliding velocity at the surface $v_x = v_s$ (m s^{-1}), normal pressure P (Pa), and IL film thickness D (m).^{115,116}

$$\mu = \frac{dF_F}{dF_N} = \frac{\sigma A}{F_N} = \frac{\eta \dot{\gamma}}{F_N} \cdot A = \frac{\eta \dot{\gamma}}{F_N/A} = \frac{\eta}{F_N/A} \cdot \frac{v_s}{D} = \frac{\eta}{P} \cdot \frac{1}{D} \cdot v_s \quad (2)$$

where σ is the shear stress (N m^{-2}), A is the area of contact (m^2), $\dot{\gamma} = dv_x(z)/dz$ is the shear rate (s^{-1}), and z is the direction normal to the surface. This equation has already been utilized to explore the quantitative interplay between nanofriction and intermolecular forces of molecular liquids at solid interfaces,¹¹⁷ yet not in ILs, and for eqn (2) to be valid, the assumption of presenting ILs between two solid surfaces needs to be held.

2.3. Slip length

Slip length, b (m), introduced by Navier in 1823,¹¹⁸ is a critical parameter to characterize the lateral dynamics of ILs at solid interfaces.^{119,120} A larger slip length indicates that the IL flow between two solid contacts experiences lower friction, and the solid moving in this IL experiences a lower drag force.

The slip length can be obtained by fitting the hydrodynamic force F_{hydro} and surface separation D measured *via* the colloid probe AFM in contact mode.^{121,122} As shown in

Fig. 4(a), the slip length b is illustrated as a “stopped layer” on each solid surface, *i.e.*, a thin liquid film in the vicinity of the solid surface with the velocity of the liquid matching that of the solid surface.

The expression for the hydrodynamic force F_{hydro} depends on the boundary condition, which can be non-slip and slip. Under the non-slip boundary condition, *i.e.*, the liquid is directly in contact with the solid surface and does not slip laterally, and the hydrodynamic force F_{hydro} on an approaching AFM colloid probe at small surface separations can be described as:¹²³

$$F_{\text{hydro}} = \frac{6\pi\eta r^2 v}{D} \quad (3)$$

where r is the colloid probe radius, D is the separation between the two surfaces at the point of the closest approaching, *i.e.*, the smallest thickness of the confined liquid film (Fig. 4a), η is the bulk viscosity of the liquid, and v is the approaching velocity of the colloid probe. While under the slip boundary condition, the hydrodynamic force F_{hydro} that allows for a slip at the interface can be formulated as:¹²⁴

$$F_{\text{hydro}} = \frac{6\pi\eta r^2 v}{D} \cdot f^* \quad (4)$$

where f^* is the correction factor for the slip at two solid surfaces with the same slip length:

$$f^* = \frac{D}{3b} \left[\left(1 + \frac{D}{6b} \right) \ln \left(1 + \frac{6b}{D} \right) - 1 \right] \quad (5)$$

When the correction factor is equal to one, *i.e.*, $f^* = 1$, eqn (4) is consistent with that for the no-slip boundary condition (eqn (3)); while $f^* < 1$ when slip occurs. Eqn (4) can be used reliably for small surface separations ($D < r$) and low Reynolds numbers. However, for IL-based systems, an additional term, F^0 , needs to be added, accounting for the effect of viscous drag on the cantilever to describe the hydrodynamic force F_{hydro} , *i.e.*,¹²⁵

$$F_{\text{hydro}} = \frac{6\pi\eta r^2 v}{D} \cdot f^* + F^0 \quad (6)$$

In general, the magnitude of F^0 is relatively small compared to the first term in eqn (6). In data processing for IL-based systems, eqn (6) is fitted to AFM approaching force curves, with f^* and F^0 as the fitting parameters.¹²⁵ Based on the obtained f^* , eqn (5) can be used to determine the slip length b . For example, Fig. 4(b) illustrates how to use the thin-film drainage data for 50 : 50 vol% mixtures of an IL propylammonium nitrate (PAN) and alcohol (butanol, hexanol, octanol, and dodecanol) in fitting with eqn (6) (*cf.* dashed lines). Subsequently, the fitted values of slip length b are presented in Fig. 4(c), varying between ~ 2 and ~ 16 nm.

The variation of slip lengths can partially and indirectly reflect the interfacial structure of ILs, *e.g.*, the ion ordering near the surface.¹²⁶ As shown in Fig. 4(d), the colloid probe AFM-obtained slip length of the IL 1-hexyl-3-methyl imidazolium bis(trifluoromethylsulfonyl)imide ($[\text{HMIM}][\text{TFSI}]$) on

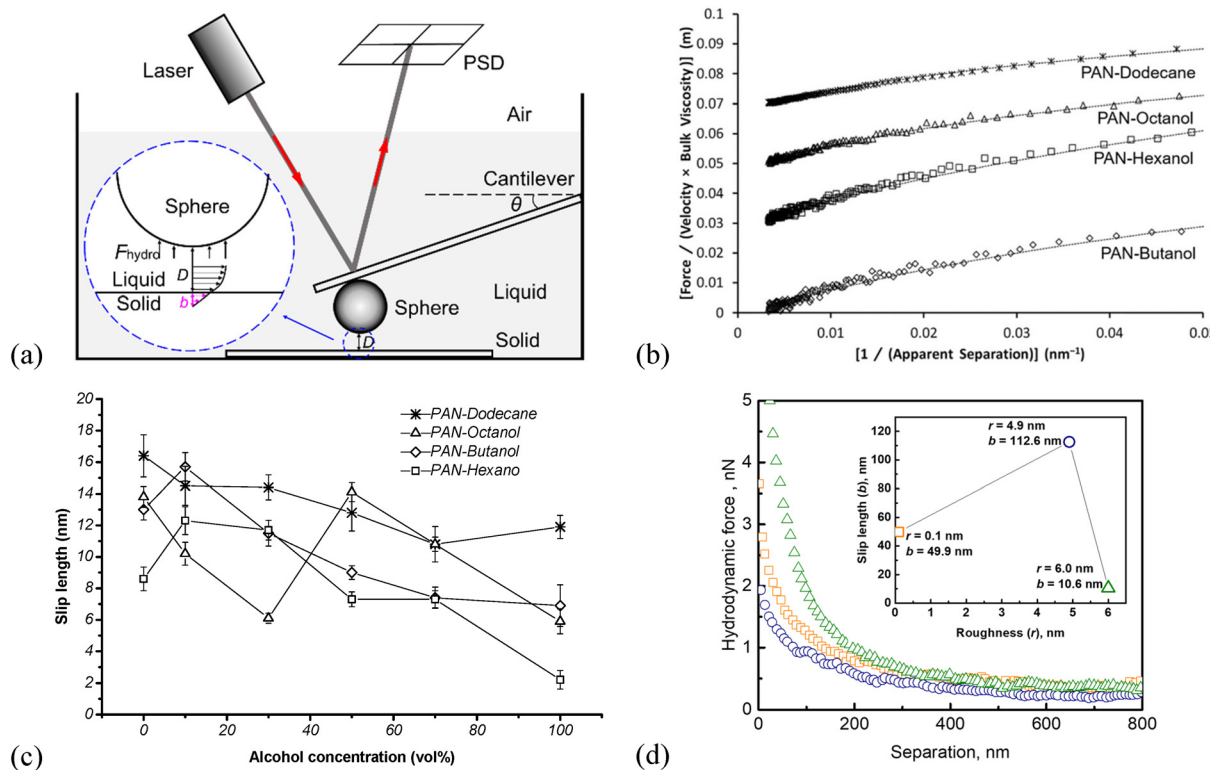


Fig. 4 (a) Schematic illustration of the slip length measurement on a solid surface using a colloidal AFM probe in contact mode. As the sphere (AFM probe) approaches the sample, liquid is driven and drained to become fluid flow.¹²¹ Copyright 2018, MDPI. (b) Thin-film drainage data for 50 : 50 vol% mixtures of an IL propylammonium nitrate (PAN) and butanol, hexanol, octanol, and dodecanol. The data are plotted as hydrodynamic force/relative velocity/viscosity as a function of 1/apparent separation. Only every 7th data point is plotted. Dashed lines are the fits using the bulk viscosity and a small slip length. The solid line intercepting butanol data represents a no-slip boundary condition using the bulk viscosity.¹²⁵ Copyright 2015, Royal Society of Chemistry. (c) The slip lengths of PAN-alcohol mixtures with varying volume concentrations of alcohol, fit using eqn (5).¹²⁵ Copyright 2015, Royal Society of Chemistry. (d) Hydrodynamic force measured with a silica colloid ($R = 4.0 \mu\text{m}$) approaching the silicon surfaces covered by silica nanoparticles (~12 nm diameter) with varying roughnesses of 0.1, 4.9 and 6.0 nm, respectively, in 1-hexyl-3-methyl imidazolium bis (trifluoromethylsulfonyl)imide ([HMIM][TFSI]) at a velocity of $10 \mu\text{m s}^{-1}$.¹²⁶ Copyright 2020, Wiley-VCH.

silicon surfaces covered by silica nanoparticles was investigated. The slip length increases as the surface roughness increases from 0.1 to 4.9 nm, associating with a weaker hydrodynamic force. While a further increase in the roughness to 6.0 nm leads to a prominent decrease in the slip length. The observed nonmonotonic change of the slip length with surface roughness is ascribed to the different ion ordering, especially at the surfaces with a roughness of 0.1 and 4.9 nm. The increased surface roughness enhances the disorder of near-surface ILs,³⁶ resulting in a decreased thickness of ordered ion layers from 8.1 Å on the smoother surface to 5.1 Å on the rougher one.¹²⁶ While a stronger force is required to squeeze-out the thinner ion layer on the rougher surface, so that these layers prevent a direct solid-solid contact to decrease the surface friction and increase the slip length. In comparison, the roughness effect outcompetes the relevance of the interfacial ion ordering on the surface with a roughness of 6.0 nm and leads to a significant decrease in the slip length.

Except for the direct acquirement by fitting the hydrodynamic force from colloid probe AFM, the slip length can also be obtained from the measured friction coefficient at liquid–solid

interfaces by conventional AFM, as reported in our previous findings.¹¹⁷ In this alternative method, the slip length b is essentially defined in terms of the fluid sliding velocity at the surface,^{127,128} v_s (m s^{-1}),

$$v_s = b \left| \frac{dv_x(z)}{dz} \right| \quad (7)$$

where x and z correspond to the directions parallel and perpendicular to the solid surface, respectively, and v_s is the sliding velocity at the surface. v_s is related to the shear stress, σ (Pa) and can be expressed as¹²⁷

$$\sigma = kv_s = \eta \left| \frac{dv_x(z)}{dz} \right| \quad (8)$$

where k (Pa s m⁻¹) is the friction factor. The comparison of eqn (7) and (8) shows that

$$b = \frac{\eta}{k} \quad (9)$$

where η (Pa s) is the liquid bulk viscosity. In fact, the slip length is related not only to the bulk viscosity but also to the

interfacial viscosity (eqn (10)).^{102,124,129} While at a very low velocity, the effect of viscosity is small on hydrodynamic forces.¹³⁰

$$b = \delta \left(\frac{\eta}{\eta_s} - 1 \right) \quad (10)$$

where δ is the thickness of the boundary layer, and η and η_s are the bulk and interfacial viscosities, respectively.

Comparing eqn (8) and (2), where the friction coefficient $\mu = \frac{\eta}{P} \cdot \frac{1}{D} \cdot v_s$, the friction factor k in eqn (5) is related by:

$$k = \frac{\mu P}{v_s} \quad (11)$$

Combining eqn (9) and (11), the slip length b is friction coefficient-dependent, *i.e.*,¹¹⁷

$$b = \frac{\eta}{\mu P} v_s \quad (12)$$

Although this proposed friction coefficient-dependent slip length has not been reported by any other groups, it offers another pathway to achieve the slip length. We believe that further development of this method in eqn (12) for obtaining the slip length with the only inputs of the experimental parameters of IL viscosity, scan velocity, normal pressure, and friction coefficient would be worth exploring more.

To sum up, both the AFM-obtained force-distance curves (section 2.1) and nanoscale friction (section 2.2) provide valuable information on local interaction force and microstructures of ILs at solid interfaces, allowing an increasing understanding of the ion arrangements in the near-surface ILs. The widespread use of the AFM as a tool for determining the slip length (section 2.3) of ILs at solid interfaces has significantly improved the mechanistic understanding of boundary slip characteristics.

3. Interfacial structure and interactions of ionic liquids affecting their properties

The properties and dynamic behavior of near-surface ILs depend on the ILs themselves, contact solid surfaces characteristics, and external conditions and stimuli, where the interfacial structuring of ILs and their interactions are important.^{35,36,131} In this section, based on AFM probing, we discuss how different types of ILs and their properties affect the microstructure and interaction of ILs at solid interfaces. The influence of solid surfaces and external stimuli on the interactions and microstructure of the interfacial ILs will be discussed in sections 4 and 5.

The microstructure of ILs at solid surfaces, including the ordering and distribution of the ions depends strongly on the species and type of the ions, which can be clearly analyzed by the AFM force curves. The number of steps and rupture forces in the force curves indicate the number of ion layers and the

strength of cohesive interactions between ions. More steps with higher rupture forces correspond to the ion layer with a stronger structure, whereas the ILs with weak structures possess few or no steps.

3.1. Interfacial structure and interaction of ILs

3.1.1 Imidazolium-based ILs. The force curve in the imidazolium-based IL 1-ethyl-3methyl-imidazolium bis(trifluoromethanesulfonyl) imide ([EMIM][Tf₂N]) at HOPG interfaces as listed in Table 1, shows distinct ion layers with the first ion layer of ~0.37 nm away from the surface of HOPG, and the subsequent ion layer of ~0.7 nm, probably consisting of a single ion or a cation-anion pair.¹³² In comparison, 1-ethyl-3-methylimidazolium trifluoromethyl-sulfonate ([EMIM][TfO]) reveals more ion layers at the Au(111) interface. The number of ion layers at [EMIM][TfO]/Au(111) interfaces increases, and the structure of ion layers is stronger under the cathodic applied surface potential, due to a better ordering of the innermost layer and a stronger near-surface structure.¹³³ The Espinosa-Marzal's group observed ~4–7 ion layers of 1-ethyl-3-methylimidazolium bis(trifluoromethylsulfonyl)imide ([EMIM][TFSI]) on graphene.¹³⁴ The Mao and Yan's group probed the ion layers of [BMIM][PF₆] based electrolyte at the Au(111) interface, arising from the ordered arrangement of [BMIM][PF₆] molecules containing both cations and anions, instead of individual cations or anions. The existence of charged interior layers and neutral exterior layers (totally 4 layers) has been further distinguished at a potential of −0.8 V. It is worthy to emphasize that the electric double layer is confined within the interior layers, resulting in the so-called charged interior layers.⁶⁷

Fig. 5 shows the influence of the cation size on the ion ordering at HOPG interfaces by varying the alkyl chain length of imidazolium ILs [EMIM][FAP], [HMIM][FAP], and [EMIM][TFSA].^{135,136} The reduction of the alkyl chain length of the cation from C₆ for [HMIM]⁺ to C₂ for [EMIM]⁺ results in more layers but smaller rupture forces. Because the shorter alkyl chain of [EMIM][FAP] compared with longer [HMIM][FAP] decreases the solvophobic interactions, resulting in lower cohesive energy within the layers and smaller rupture forces. For ILs with the same cation [EMIM]⁺, the number of ion layers and the associated rupture forces are lower in the case with smaller [TFSA][−] anions than larger [FAP][−], indicating weaker ion ordering, while the energetic origin of this effect is still unclear. It is likely because replacing the larger [FAP][−] with the smaller [TFSA][−] hinders the packing of ions into layers, or leads to a weakened solvophobic interaction.¹³⁶ The effect of variation in the cation alkyl chain length on IL microstructures was also examined at the polarized Au(111) surfaces for the ILs [EMIM][FAP], [HMIM][FAP] and [BMIM][FAP] (1-butyl-3-methylimidazolium tris(pentafluoroethyl)-trifluorophosphate).¹³⁵ [HMIM][FAP] with the longest cation alkyl chain produces the strongest solvophobic force, increasing the cohesive forces within layers and resulting in the strongest layering structure. [BMIM][FAP] shows the weakest structure with the lowest rupture forces. [EMIM][FAP] with the shortest

Table 1 Comparison of ion layers in the imidazolium and nitrate-based ILs at the mica interfaces (blue for approach, red for retraction part)

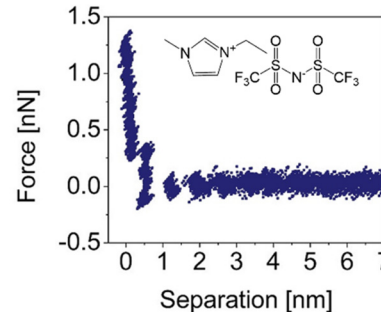
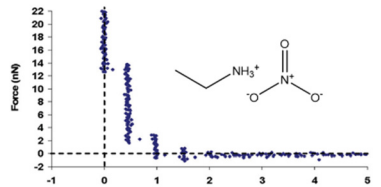
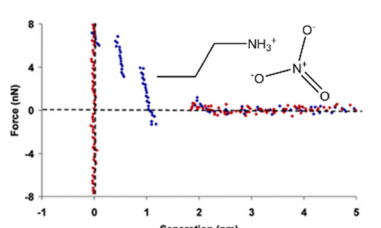
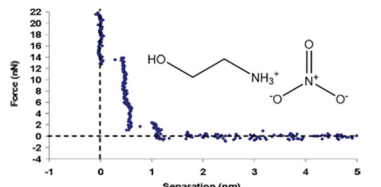
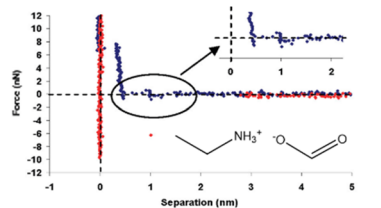
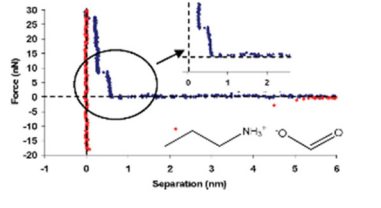
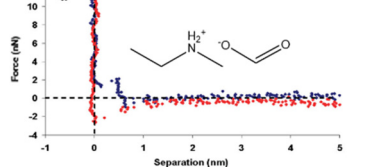
Full name of ILs	Abbreviation	Number of ion layers
1-Ethyl-3methyl-imidazolium bis(trifluoromethanesulfonyl)imide ¹³² Copyright 2013, American Chemical Society	[Emim][Tf ₂ N]	
Ethylammonium nitrate ¹³⁹ Copyright 2009, American Chemical Society	EAN	
Propylammonium nitrate ⁴³ Copyright 2007, American Chemical Society	PAN	
Ethanolammonium nitrate ¹³⁹ Copyright 2009, American Chemical Society	EtAN	
Ethylammonium formate ¹³⁹ Copyright 2009, American Chemical Society	EAF	
Propylammonium formate ¹³⁹ Copyright 2009, American Chemical Society	PAF	
Ethylmethylammonium formate ¹³⁹ Copyright 2009, American Chemical Society	EMAF	

Table 1 (Contd.)

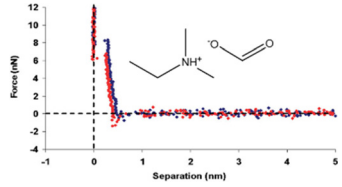
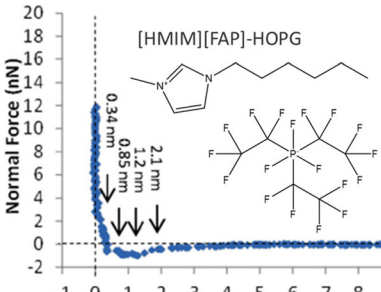
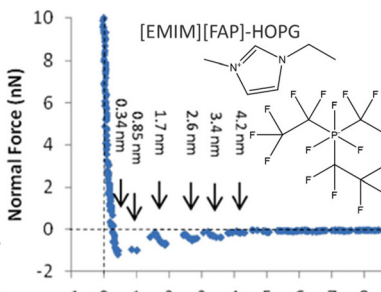
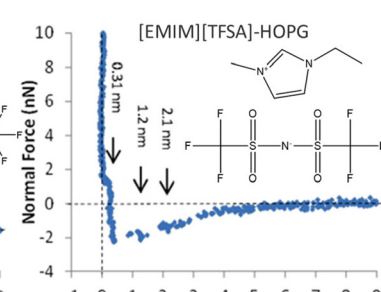
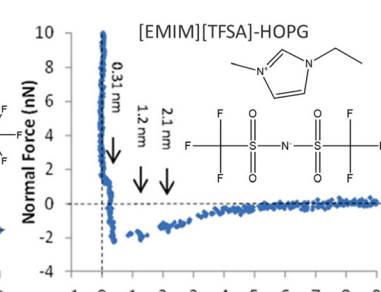
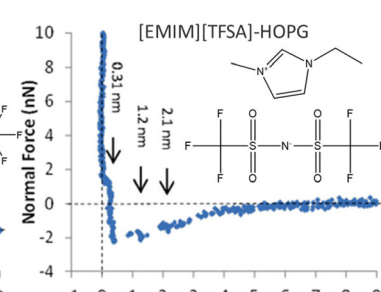
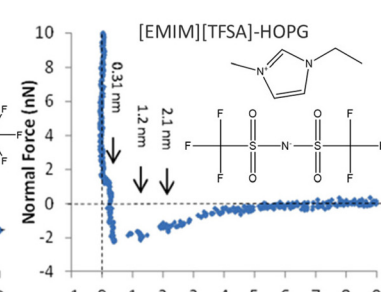
Full name of ILs	Abbreviation	Number of ion layers
Dimethylethylammonium formate ¹³⁹ Copyright 2009, American Chemical Society	DMEAF	
	[HMIM][FAP]-HOPG	
	[EMIM][FAP]-HOPG	
	[EMIM][TFSA]-HOPG	

Fig. 5 Force curves (the approach part) for a sharp silicon probe approaching an HOPG surface in ILs [HMIM][FAP], [EMIM][FAP], [EMIM][TFSA].¹³⁶ Copyright 2014, IOPscience. [HMIM][FAP] = 1-hexyl-3-methylimidazolium tris(pentafluoroethyl)tri-fluorophosphate, [EMIM][FAP] = 1-ethyl-3-methylimidazolium tris(pentafluoroethyl)tri-fluorophosphate, [EMIM][TFSA] = 1-ethyl-3-methylimidazolium bis(trifluoromethylsulfonyl)imide.

cation alkyl chain has a stronger structure than [BMIM][FAP], because the imidazolium ring of $[\text{EMIM}]^+$ cations orients more parallel than $[\text{BMIM}]^+$ to the Au(111) surface, which is favourable for the templating structure. The surface bound cations are found to be more effective than $[\text{FAP}]^-$ anions for inducing these ion structures at interfaces, because the rupture forces are observed to be higher at negative potentials than at positive potentials, indicating a stronger structure at the cation-rich surface.

3.1.2. Ammonium-based protic ILs. The AFM approaching force curve for the EAN/mica system in Table 1 exhibits a series of steps, with the first step, corresponding to the ion layer closest to the negatively charged mica, attributed to the cation-rich layer with the NH_3^+ group orientated toward mica and ethyl tails facing the bulk liquid. The second step is a cation–anion pair with the alkyl chains orientated towards the tails of the first layer, with the NO_3^- anion facing towards the third layer, and so on. The variation of ion sizes can influence the ion layering next to the solid surface because of the different interaction forces among the ions.¹³⁷ For example, increasing the size of the hydrocarbon moiety of the IL from C_2 in EAN to C_3 for PAN significantly increases the force magnitude and reduces the number of ion layers (Table 1). Greater attractive forces of longer PAN with mica are detected due to the longer alkyl chain of PAN producing stronger solvophobic segregation.¹³⁸ The force steps in PAN are not vertical like those in EAN, suggesting that these detected ion layers in PAN are more compressible, *i.e.*, less pronounced ion ordering.⁴³ By introdu-

cing an OH group to the cation-alkyl tail in EAN to form EtAN, the number of the ion layers is reduced from 4 to 3. This is because the OH group lowers the cohesive forces within the layers by disrupting the solvophobic attractions, producing fewer, less well-defined layers. Replacing the NO_3^- anion of EAN with formate (EAF and PAF) further reduces the number of ion layers to 2 layers. This also results in distinct cation and anion sublayers (magnified panels in Table 1). In comparison with PAF, the number of ion layers in EMAF and DMEAF is further reduced to 1 layer when the primary cations are substituted by the secondary or tertiary ammonium ones, weakening the cation layer adsorption onto mica.¹³⁹

3.1.3. Solvated ILs. The effects of anion type and glyme chain length on the structure of solvate ILs (SILs) ($\text{Li}(\text{G3})\text{TFSI}$, $\text{Li}(\text{G4})\text{TFSI}$, $\text{Li}(\text{G4})\text{BETI}$, $\text{Li}(\text{G3})\text{TFA}$, $\text{Li}(\text{G1})_2\text{TFSI}$, see Table 2) were investigated at the HOPG interfaces by the Atkin's group.¹⁴⁰ They found less structured ion layers in $\text{Li}(\text{G4})\text{BETI}$ than in $\text{Li}(\text{G4})\text{TFSI}$ because of the longer carbon chain in $[\text{BETI}]^-$ leading to the increased conformational flexibility. $\text{Li}(\text{G3})\text{TFA}$ shows weaker interfacial structures due to the higher coordination strength of $[\text{TFA}]^-$ with Li^+ . For the SILs with the same anions, $\text{Li}(\text{G3})\text{TFSI}$ shows the strongest structure, followed by $\text{Li}(\text{G4})\text{TFSI}$ and $\text{Li}(\text{G1})_2\text{TFSI}$, due to the rigid cation complex formation as all the coordination sites on the solvate (G3) being occupied. Replacing G3 with longer G4 results in more flexible $[\text{Li}(\text{G4})]^+$ cations in $\text{Li}(\text{G4})\text{TFSI}$ and thus a weaker structured ion layer. $\text{Li}(\text{G1})_2\text{TFSI}$ exhibits the weakest structure because of the poor solvation interactive strength of G1.¹⁴⁰

Table 2 Molecular structures of solvate ILs: gray-Li, cyan-C, red-O, blue-N, yellow-S, orange-F¹⁴⁰ Copyright 2017, American Chemical Society

Full name of solvate ILs	Abbreviation	Molecular structure
Lithium triglyme bis(trifluoromethylsulfonyl)imide	Li(G3)TFSI	
Lithium tetraglyme bis(trifluoromethylsulfonyl)imide	Li(G4)TFSI	
Lithium tetraglyme bis(perfluoroethylsulfonyl)imide	Li(G4)BETI	
Lithium triglyme trifluoroacetate	Li(G3)TFA	
Lithium di-monoglyme bis(trifluoromethylsulfonyl)imide	Li(G1) ₂ TFSI	

3.1.4 Phosphonium-based and amphiphilic ILs. No interfacial stratification is observed in the phosphonium-based IL with a longer cation chain. For example, as shown in the left panel of Fig. 6, trihexyl(tetradecyl)phosphonium bis(mandelato)borate ($[P_{6,6,6,14}][BMB]$) only exhibits a monotonic repulsion with a characteristic steric decay length on mica, which is comparable with the size of the ions, suggesting the formed layers are diffuse. The lack of steps is probably caused by the long alkyl chains of the cation, the large size of the anion, and the crowding of the cations at the surface of negatively charged mica.¹⁴¹ Similarly, no steps was observed for trihexyl(tetradecyl)phosphonium bis(2,4,4-trimethylpentyl)phosphinate ($[P_{6,6,6,14}][(^3C_8)_2PO_2]$) and trihexyl-(tetradecyl)phosphonium bis(trifluoromethane)sulfonamide ($[P_{6,6,6,14}][TFSI]$) at stainless steel surfaces (Fig. 7a, middle and right), due to the surface roughness and the weakened electrostatic interaction of $[P_{6,6,6,14}]^+$ with the anion caused by the bulkiness of the

cation.⁵¹ In contrast, the shorter-chained phosphonium based IL, e.g., tributyl-(methyl)phosphonium bis(trifluoromethane) sulfonamide ($[P_{4,4,4,1}][TFSI]$), shows clear force steps (Fig. 6, right panel).⁴⁷

Fig. 7 compares ion layers for amphiphilic and non-amphiphilic ILs⁸ at the graphite surfaces with an applied potential of -1 V . The IL 1-butyl-3-methylimidazolium 1,4-bis(2-ethylhexoxy)-1,4-dioxobutane-2-sulfonate ($[C_4C_1Im][AOT]$) is amphiphilic with a special anion $[AOT]^-$, which is distinctly amphiphilic with a negative charge located at one end of the ion (polar head) and a bulky branched di-chain hydrocarbon group at the other end (non-polar tail) (Fig. 7a, inset on top). The control IL is a common non-amphiphilic IL, 1-butyl-3-methylimidazolium tetrafluoroborate ($[C_4C_1Im][BF_4]$), that contains an identical cation to $[C_4C_1Im][AOT]$ but a smaller, inorganic anion (Fig. 7b, inset on top). Both curves in Fig. 7 consist of at least four pronounced, discrete steps (I, II, III, and IV), produced by the probe pushing up against and rupturing ion layers. Noting that the rupture force for step I is higher for $[C_4C_1Im][AOT]$ than for $[C_4C_1Im][BF_4]$ at both OCP and -1 V , indicating that the number density of the innermost layer is much larger in $[C_4C_1Im][AOT]$.

The amphiphilic $[C_4C_1Im][AOT]$ exhibits an unusual interfacial ion distribution, resulting from significant van der Waals interactions owing to the non-polar surfactant tails in the anion (Fig. 7a, inset). The polar heads of anions $[AOT]^-$ are electrostatically attracted to the interface at a positively charged graphite surface, whereas the non-polar tails orientate outward, in close proximity to the non-polar tails of the next anion layer. A bilayer forms parallel to the positively charged surface, with a neutralizing cation layer adjacent to the anionic polar heads. Near a negatively charged surface, the innermost ion layer is enriched in cations, fully neutralizing the adjacent anionic bilayer. In contrast, most cations and anions in the conventional non-amphiphilic IL $[C_4C_1Im][BF_4]$ prefer to form ‘neutral aggregates’ (Fig. 7b, inset) in the electric double layer because the ion distribution is dominated by the coulombic interactions. The notably different separation between the

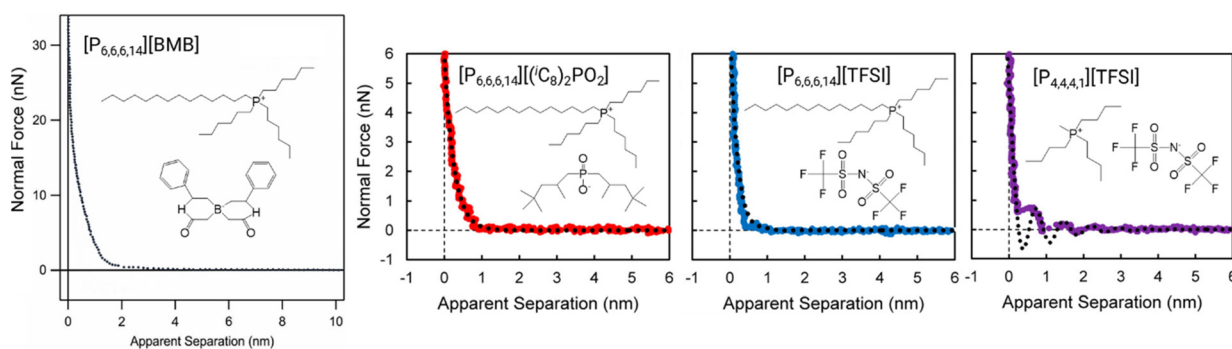


Fig. 6 Typical force curves in phosphonium-based ILs: $[P_{6,6,6,14}][BMB]$ confined between diamond-like carbon-coated AFM probe and mica,¹⁴¹ Copyright 2018, MDPI. $[P_{6,6,6,14}][(^3C_8)_2PO_2]$, $[P_{6,6,6,14}][TFSI]$ and $[P_{4,4,4,1}][TFSI]$ confined between a silicon AFM probe and a stainless steel surface.⁵¹ Copyright 2017, American Chemical Society. The dotted lines in $[P_{6,6,6,14}][(^3C_8)_2PO_2]$, $[P_{6,6,6,14}][TFSI]$ and $[P_{4,4,4,1}][TFSI]$ are the fits using a model developed by Hoth *et al.*, describing the interaction potential approaching the surface, which is not discussed in this review.¹⁴² Copyright 2014, IOPscience.

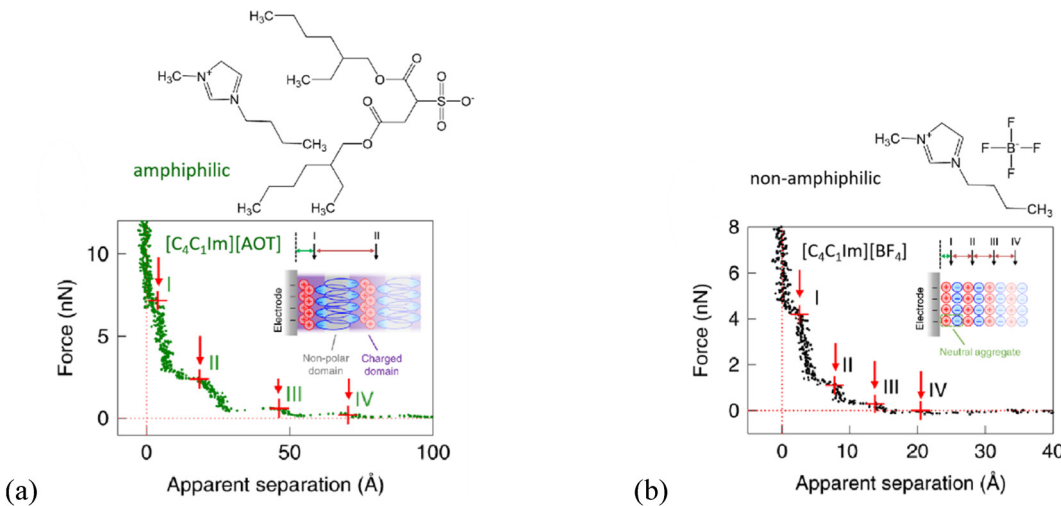


Fig. 7 AFM force versus separation profiles obtained with a silica colloid probe approaching a graphite electrode surface immersed in (a) $[C_4C_1\text{Im}][\text{AOT}]$ and (b) $[C_4C_1\text{Im}][\text{BF}_4]$ with applied potential of -1 V .⁸ Copyright 2019, Springer Nature. The insets on top are molecular structures of the ILs 1-butyl-3-methylimidazolium 1,4-bis(2-ethylhexoxy)-1,4-dioxobutane-2-sulfonate $[C_4C_1\text{Im}][\text{AOT}]$ and 1-butyl-3-methylimidazolium tetrafluoroborate $[C_4C_1\text{Im}][\text{BF}_4]$. Red crosses marked I, II indicate the locations of each discrete step and the 'rupture force' magnitudes.

graphite surface and step I (the nearest ion layer at the surface) for non-amphiphilic $[C_4C_1\text{Im}][\text{BF}_4]$ and amphiphilic $[C_4C_1\text{Im}][\text{AOT}]$ confirms the different ion structures. The separation between graphite surface and step I for amphiphilic $[C_4C_1\text{Im}][\text{AOT}]$ is about 4 \AA , corresponding to a cation-rich layer (Fig. 7a, green double arrow). For non-amphiphilic $[C_4C_1\text{Im}][\text{BF}_4]$, the separation is about 2–3 \AA , indicating a single ion layer (Fig. 7b, green double arrow). These observations *via* AFM force curves provide evidence for a strong influence of molecular configuration of cations and anions on the IL microstructure at interfaces.

To briefly summarize, the microstructure of ILs near the solid surface is sensitive to both cation and anion structures, and the ion layers of ILs at solid interfaces can be tuned by modifying the cation and anion molecular structures to control the geometrical packing, and electrostatic attractions, *etc.*¹³⁹ Both fewer and more layers were observed for the ILs with increased molecular flexibility in cations or anions,^{43,139} and the ion layering could be disrupted by weakening the layered ion structure that creates solvophobic segregation, or by increasing the bulkiness of the cations, which hinders packing into layers.¹³⁹ This provides a guideline for the “bottom-up design and optimization of ILs for diverse technologies including heterogeneous catalysis, lubrication, electrochemical processes, and nanofluids”.¹³⁸

3.2. Nanofriction of interfacial ILs

The structured ion layers can change the properties and alter the nanofriction of sliding surfaces across IL films.^{53,143} On the macroscale, the pyridinium-based ILs result in lower friction than imidazolium-based ILs,¹⁴⁴ and the friction coefficient was observed to decrease with an increasing alkyl chain length for both imidazolium and pyridinium cations, because

of the increased IL viscosity to prevent direct solid–solid contact.^{144,145} On the nanoscale, the friction is more sensitive to the variation in ionic structures rather than the surface asperities and roughness, because the influence of the latter ones is reduced at the nanoscale.⁵³ Recently, shorter alkyl chains of the cation were found to be preferred for lowering the nanoscale friction,^{53,146} *e.g.*, in the ILs 1-*n*,2-methylimidazolium tetrafluoroborate $[C_n\text{MIM}][\text{BF}_4]$ (*n* = 2, 4, 6, Fig. 8a). The IL containing a cation with a shorter aliphatic chain shows a smaller friction force, while the cation with a longer chain is more resistant to squeeze-out by external loads.^{146,147} This stronger ion structure of the longer-chained IL is also confirmed by the lower mobility observed in the IL with longer alkyl chains at the mica surface due to the stronger solvophobic interaction force.¹⁴⁸ Espinosa-Marzal and Spencer *et al.* further proposed nanoscale Stribeck curves to describe the nanofriction behavior of ILs at solid interfaces, which distinguish three lubrication regimes, *i.e.*, boundary-film, intermediate, and hydrodynamic lubrication regimes.¹⁴⁷

Atkin’s group found that in the hydroxy-functionalized ILs, the interfacial lubrication relates strongly to the cation bilayer structure caused by the formed H-bonding, which can be well-controlled *via* the alkyl chain length, the cation charge polarizability, and the coordination strength of the anions (Fig. 8b). Compared with the similar conventional ILs, the hydroxy-functionalized ILs prefer to form the cation bilayer structure due to the formation of H-bonds, enhancing the ion ordering and thus improving the interfacial lubrication.¹⁰³ In Fig. 8(c), a dicationic IL, 1,10-bis(3-methylimidazolium)decane di[bis(trifluoromethylsulfonyl)-imide] confined by mica, shows a layered nanofriction behavior accompanied by a layered ion structure. As the normal load F_N increases, an IL layer is squeezed out, leading to a smaller surface separation D and a

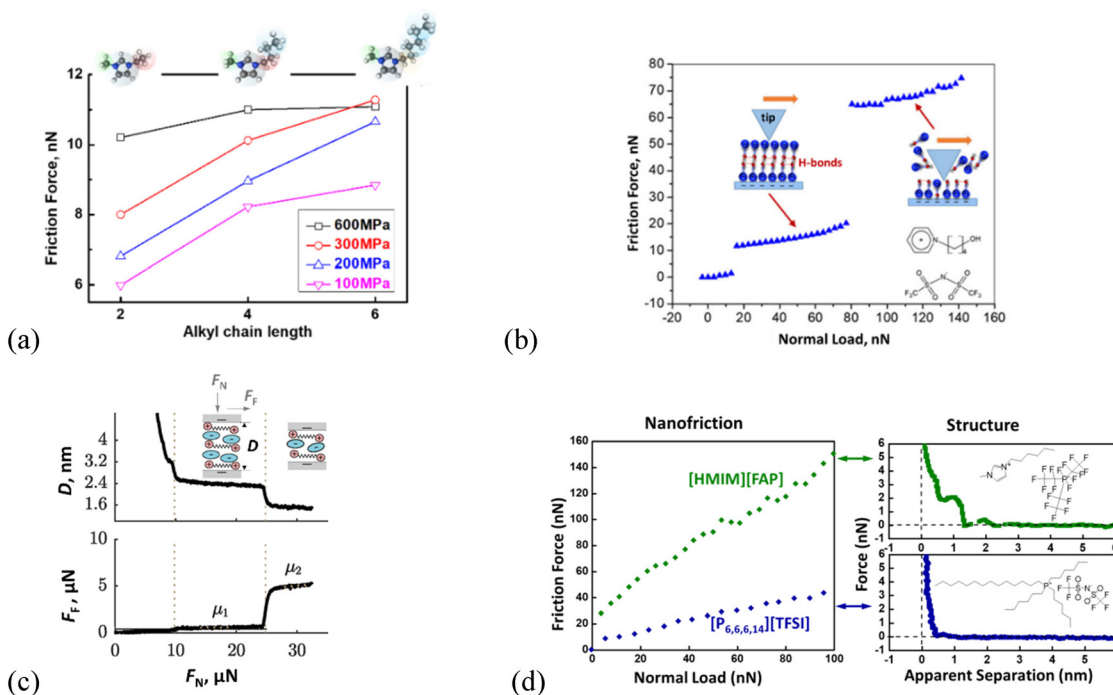


Fig. 8 (a) Friction force as a function of the alkyl chain length in IL cations for different normal loads (anion is $[\text{BF}_4]^-$).¹⁴⁶ Copyright 2020, American Chemical Society. (b) Friction force vs. normal load of the IL, 1-(4-hydroxybutyl)pyridinium bis(trifluoromethanesulfonyl)imide, $[\text{HOC}_4\text{Py}][\text{NTf}_2]$ at mica surfaces.¹⁰³ Copyright 2020, American Chemical Society. (c) Surface separation D and friction force F_F as a function of normal load F_N during friction measurements for the dicationic IL, 1,10-bis(3-methylimidazolium)decane di[bis(trifluoromethylsulfonyl)-imide] on mica.¹⁴⁹ Copyright 2019, American Chemical Society. (d) Friction force vs. normal load and force curves of the ILs, 1-hexyl-3-methylimidazolium tris(pentafluoroethyl) trifluorophosphate ($[\text{HMIM}]^+[\text{FAP}]^-$) and trihexyl(tetradecyl)phosphonium bis(trifluoromethane) sulfonamide ($[\text{P}_{6,6,6,14}]^+[\text{TFSI}]^-$) for a sharp silicon AFM probe sliding on a stainless steel surface.⁵¹ Copyright 2017, American Chemical Society.

larger friction force F_F , and the resulting friction coefficients (μ_1, μ_2) depend on the number of squeeze-out IL layers.¹⁴⁹ In particular, an unusual negative friction-load dependence, in which the friction reduces at a higher load, is observed in the phosphonium-based ILs on titanium. This is because of the ion structural reorientation promoted by the acceleration of the ion diffusion.²⁸ The enhanced ion diffusion leads to an increase in the near-surface mobility of ions, promoting the structural change of cations into a flat orientation as the probe penetrates the ion layer at higher loads. The resulting flat orientation favors the decrease of the friction force at higher loads than at lower loads, namely, the negative friction-load dependence.

However, the influence of the ion layers on nanofriction at IL–solid interfaces is still controversial. Perkin's group found an increased nanofriction as the number of ion layers decreases for the IL confined between two mica sheets. They explained that the layers closer to the mica surfaces are more ordered, with a greater ion excess concentration, resulting in a stronger ‘inter-layer attraction for the same value of contact area and a greater activation barrier for unlocking the surfaces to allow shear’.⁵⁰ Atkin's group confirmed that the nanofriction and the degree of interfacial ILs microstructure are inversely correlated at stainless steel surfaces (*cf.* Fig. 8d).⁵¹ We recently reported a similar finding, in which the nanoscale

friction coefficient increases monotonically as the ion layers decrease.⁵² However, Atkin's group^{53,54} also found a different effect of the ordered IL layers on the friction coefficient, *i.e.*, more ordered IL layers lead to a smoother sliding plane and reduced friction coefficient. The observed decreasing friction force at the surface with stronger ion ordering was further confirmed by simulation findings.¹⁵⁰ Thus, it is a controversy over the effect of ordered IL layers on the friction coefficient at IL–solid interfaces, which needs to be investigated further.

4. The effect of surface properties on ionic liquid structuring and interactions

4.1. Planar solid surfaces

Many investigations consider the surfaces of mica, graphite, silica, and gold as the model planar surfaces to examine how the surface affects the IL structuring and interactions. For example, in the case of highly charged, atomically smooth mica, the greatest number of ion layers is observed for EAN (section 3.1.2, Table 2). While on silica, the repulsive peaks of EAN are smeared considerably, producing fewer ion layers than on mica (left panel in Fig. 9). The force profile for EAN

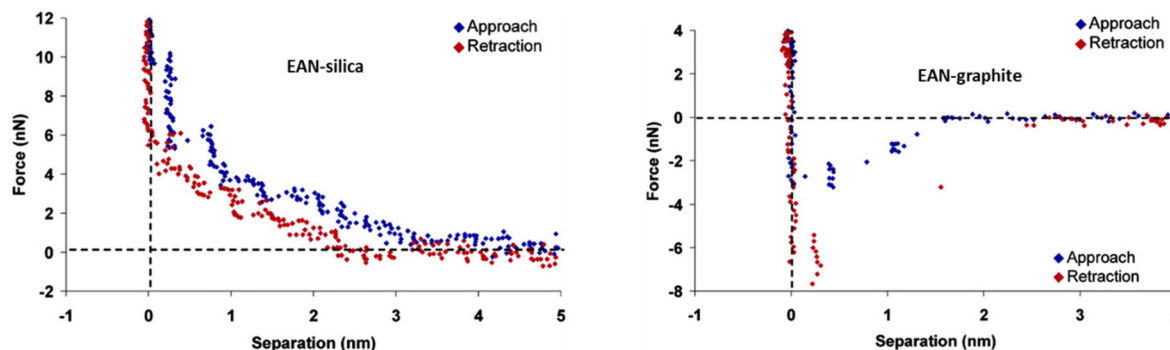


Fig. 9 Force curves for AFM Si_3N_4 probe approaching and retracting on silica and graphite surfaces in the IL EAN.⁴³ Copyright 2007, American Chemical Society.

on graphite has a very different form compared with that on mica and silica. As shown in the right panel in Fig. 9, only two ion layers of EAN are detected on graphite against an attractive background. This is because that graphite is atomically smooth, but an attraction between the surface and AFM probe occurs. Subsequently, for graphite, two adhesion forces are detected on retraction, including the force between the AFM probe and the surface (-7 nN), and the force between the probe and the adsorbed cation layer at a separation of 0.35 nm (-7.5 nN). The existing attractive probe–substrate force results in lower forces required to rupture the interfacial layer on graphite compared with that on mica.⁴³ Espinosa-Marzal's group specifically studied the effect of underlying solid supports (graphene, silica, gold) on the ion structures of imidazolium-based ILs. They found that the number of ion layers on graphene is more than those on silica and gold supports ($\sim 3\text{--}4$ layers), partially due to the atomically smooth graphene plane favorable for the ion layering enhancement than the relatively rough silica and gold.¹³⁴

The presence of a solid surface makes the interfacial ILs arrange into more ordered ion layers,²² and such layered ILs at the planar solid surfaces can dramatically impact the nanoscale friction behavior. For example, the friction coefficients of $[\text{BMIM}]^+[\text{BF}_4]^-$ and $[\text{BMIM}]^+[\text{PF}_6]^-$ on HOPG and mica were found to increase monotonically as the thickness of near-surface ordered ion layers decreases. The layering of IL ions can extend to tens of nanometers on the mica surface, while only nanometer-sized and less ordered IL domains form on HOPG,⁵² similar to the finding in the earlier work,¹⁵¹ because of a stronger coulombic force between the IL and mica surface.¹⁵² Noting that such a thick ion layer is not always observed on the mica surface,^{43,153} as the coulombic force also depends on the structure of ILs.⁹¹ For example, the IL, 1-ethyl-3-methylimidazolium acetate, forms 7 ion layers on the HOPG surface, whereas the same IL has only 3 ion layers on the mica surface.⁴³ As the HOPG surface has no charge, the coulombic force cannot be responsible for the ion layers, indicating that there must be other mechanisms.¹⁵² The comprehensive effects of surface charges on the interfacial structuring and interactions of ILs are discussed in section 5.2.

4.2. Heterogeneous solid surfaces

Surface heterogeneities, including the surface roughness and charges, are critical determinants of the solvation layer formation in ILs, and this part only focuses on the effect of the surface roughness. The layered IL structures can be disrupted by the surface roughness due to the entrapment of the IL molecules at the rough contact,^{36,91} and the roughness even slightly exceeding the ion dimensions can smear the interfacial forces.^{36,154,155} To characterize the heterogeneity of silica surfaces on the structuring of ILs, Espinosa-Marzal's group captured force isotherms with differently roughened silica colloid probes (RMS = 2, 9 nm) on 1-hexyl-3-methylimidazolium bis(trifluoromethylsulfonyl)imide ($[\text{HMIM}]^+[\text{NTf}_2]^-$).³⁶ As shown in Fig. 10(a), the interfacial IL layering is resolved in most of the measured force isotherms with both colloid probes (RMS = 2, 9 nm). The layered structure is most pronounced near the solid surface but decays with distance from the substrate surface and typically vanishes beyond ~ 3 layers. In the case of the smoother colloid probe (RMS = 2 nm), the substrate roughness plays a significant role in determining the interfacial structure of the IL, in which, the number of resolved layers decreases as the surface roughness increases (RMS: $0.4 \rightarrow 1.8 \rightarrow 4 \text{ nm}$), *i.e.*, a less ordered IL on a rougher substrate surface (top panel, Fig. 10a). With a rougher colloid probe (RMS = 9 nm), it demonstrates a less pronounced order of the IL on the rougher substrates (bottom panel, Fig. 10a).

The influence of nanoscale roughness on nanofriction is intricate. For example, the friction of an IL confined between carbon-based surfaces was found to increase with the geometrical roughness of each surface, but this increase is more sensitive at lower roughness values, even at atomic scales.¹³¹ Also, the roughness effect on nanofriction is dependent on the contact stress.¹²⁶ For 1-hexyl-3-methylimidazolium bis(trifluoromethylsulfonyl)imide ($[\text{HMIM}]^+[\text{TFSI}]^-$) on the silicon surfaces, when applied high stresses by sharp AFM probes ($<10 \text{ nm radius}$, Fig. 10b, left panel), 3 different linear regions (I, II, and III) are observed on the surface with a roughness of 0.1 nm as the load increases, while only one linear friction-

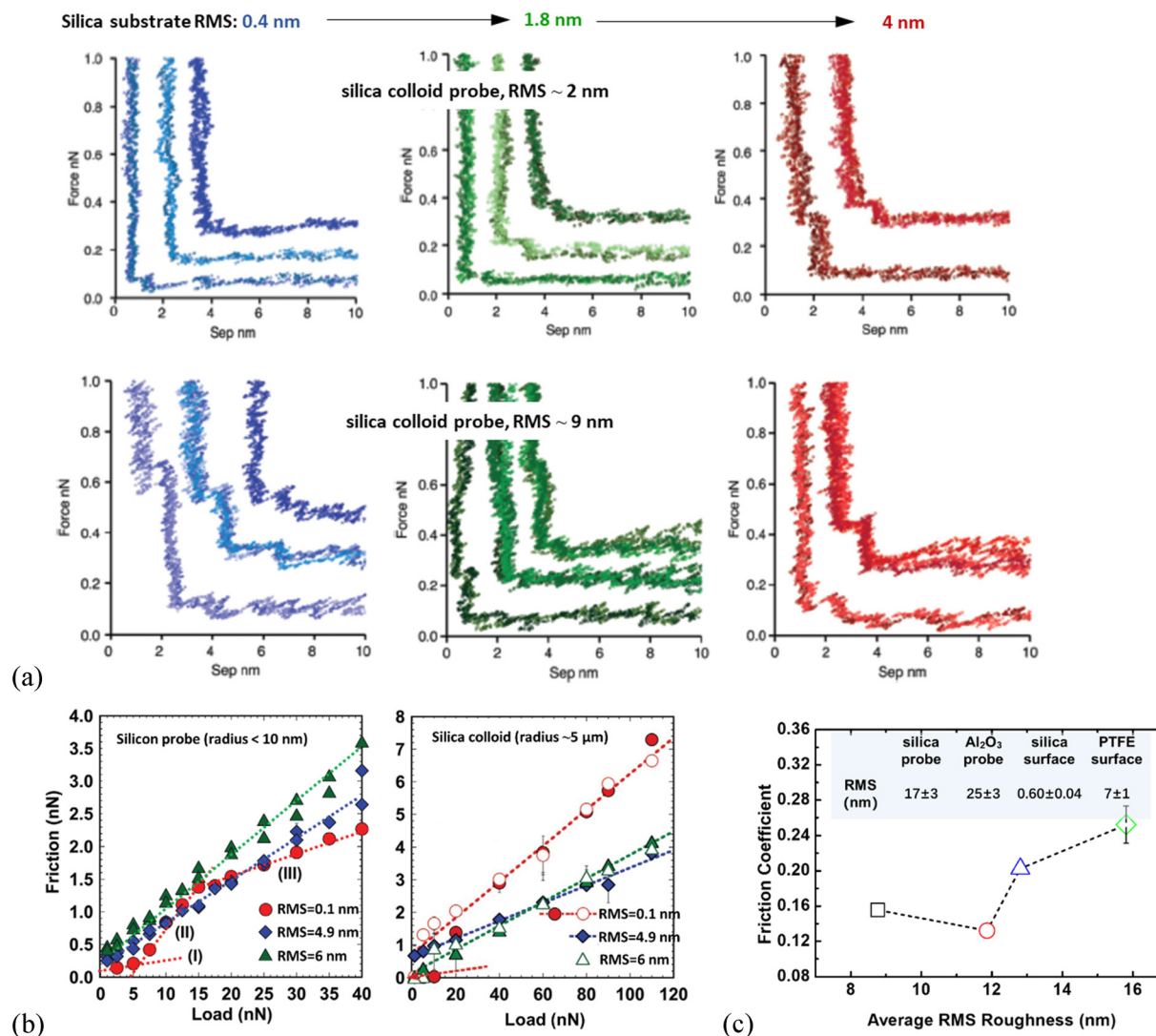


Fig. 10 (a) Representative force curves of 1-hexyl-3-methylimidazolium bis(trifluoromethylsulfonyl) imide ($[HMIM][NTf_2]$) obtained with a smooth (RMS = 2 nm) and rough (RMS = 9 nm) silica colloid probes (diameter of 10 μm) on silica substrates with varying roughness (RMS = 0.4, 1.8, 4 nm). In each panel, different colors corresponding to the force curves on the same substrate measured at different positions.³⁶ Copyright 2016, Royal Society of Chemistry. (b) Friction versus normal load on nano-roughened silicon surfaces lubricated by the IL 1-hexyl-3-methylimidazolium bis(trifluoromethylsulfonyl) imide ($[HMIM][TFSI]$) using sharp AFM silicon probe (left), and silica colloid probe (right).¹²⁶ Copyright 2020, Wiley-VCH. (c) Friction coefficient for the IL ethylammonium nitrate (EAN) between varying nano-roughened solid interfaces: silica and Al_2O_3 colloid probes sliding on the substrates, silica, and PTFE. Here the average RMS roughness is a "combined" RMS roughness estimated by arbitrarily averaging the roughness of the probe and that of the substrate (from left to right: silica–silica, silica–PTFE, Al_2O_3 –silica, and Al_2O_3 –PTFE).¹⁵⁶ Copyright 2012, American Chemical Society. The inset in (c) shows the RMS roughness for surfaces and probes taken over 1 \times 1 μm area AFM images.

load region appears on the two rougher surfaces (roughness: 4.9 and 6 nm). On the smoothest surface, regime I at the lowest load is associated with the multilayer slip, enabling the reduction of friction coefficient, while regimes II and III at higher loads correspond to the ion monolayer adsorbed onto surfaces. A transition from region I to II happens upon an applied normal load of 5 nN associating with an increased friction coefficient. A slight structural transition with a smaller friction coefficient is observed from region II to III upon a further increase in the load, due to the smoothening surface-adsorbed IL ions at a higher load. While the observed higher

friction coefficient in region II is ascribed to the rougher slip plane of the adsorbed monolayer which has not been fully compressed in the loading range of region II. The detected frictional characteristic is completely different at the same $[HMIM][TFSI]$ –silicon interfaces with much smaller contact stresses provided by larger silica colloid probes ($\sim 5 \mu m$ radius, Fig. 10b, right panel). On the smoothest surface, the friction force does not increase linearly with the load (solid circles), and only a single friction-load linear region is detected in replica experiments (roughness of 0.1, 4.9, 6 nm) (open circles).

In an earlier experimental study, the friction coefficient was found to increase monotonically with the roughness of contacts mediated by the IL, EAN, using the AFM colloid probes (Fig. 10c).¹⁵⁶ While molecular dynamics simulations have shown that the friction at contacts lubricated by ILs can both increase¹⁵⁷ and decrease¹⁵⁸ with increasing surface roughness. The increase in the friction for the rough case is explained as a result from the lateral ordering of the IL ions inside the valleys of the rough surface,¹⁵⁷ which requires a greater activation barrier to be overcome to unlock the surfaces to allow shear,⁵⁰ and hence increases the friction force. In contrast, the friction is found to decrease on a rough surface which is modeled by introducing two asperities with truncated cone geometry, due to the slightly lower tangential component for the rough surface. While the higher tangential component on the atomically flat surface is indicative of a higher normal load, and at this situation, it is more difficult to approach two flat surfaces than two rough ones being associated with the highly ordered adsorbed ion layer at the flat surface.¹⁵⁸ The different simulation predictions apparently highlight the sensitivity of the friction to the surface structure at the molecular level. Noting that the modeling roughness in the former case is only 1 nm,¹⁵⁷ corresponding to a smooth surface in the experimental work. Thus, it is necessary to build a more realistic rough surface by taking into account the presence of surface inhomogeneities and asperities characteristic of real surfaces, to examine the roughness impact on the friction. Compared to the friction, a nonmonotonic change of the slip length with the nano-roughness has also been reported simultaneously, where the slip length at the [HMIM][TFSI]-silicon interface with an RMS roughness of 4.9 nm is significantly larger than that on the surface with a roughness of 0.1 nm. However, the [HMIM][TFSI] coated surface with an RMS roughness of 6 nm led to considerably smaller slip length than that on the smooth surface.¹²⁶ The dependence of slip on the surface roughness^{159,160} offers a way to control IL hydrodynamics by designing the underlying material, while this is not available for the material-independent non-slip boundary condition.

Except for the surface roughness, the chemical composition of the surface also influences the structure and

dynamics of ILs at solid interfaces.¹⁶¹ A solid surface functionalized by 3-hydroxytyramine hydrochloride was found to enable the catecholic anchor of imidazolium ILs to improve the nanofrictional performance of the surface.¹⁶² With the fraction of hydroxylation in graphene oxide (GO) increasing from 0 to 15%, the friction coefficient of [BMMI][BF₄] confined in GO nanochannels can be enhanced by almost 60 times, and the slip length can be reduced by 3 orders of magnitude. This sensitive change of friction coefficient and slip length to the surface hydroxyls is ascribed to the changing structure in the first dense IL layer close to the GO wall.¹⁶³

5. Effect of external stimuli on the interaction and microstructure at ionic liquid–solid interfaces

5.1. Temperature

The number, location, and shape of oscillatory structural forces in molecular liquids and the bulk ILs are fairly insensitive to small changes in temperature.²² While this does not hold for the near-surface ILs, *e.g.*, the force curves of the EAN-mica system show a significant temperature dependence,^{41,139} even though that of confined molecular liquids is insensitive to the temperature.¹⁶⁴ The number of ion layers for various room temperature ILs on mica is found to decrease with increasing temperature, and the forces required to rupture through each of the layers decrease.¹³⁹ In Fig. 11(a), the number of ion layers in EAN decreases from 7 to 4 layers as the temperature increases from 14 to 30 °C, and the force required to rupture the innermost ion layer decreases by more than half. These decreased number of ion layers and rupture force are ascribed to the increased thermal motion of ions, disrupting solvophobic attractions between cation alkyl groups and thus weakening the IL structuring.⁴¹ The temperature-dependent interfacial layering structure was also observed earlier in the fluorinated ILs at a charged sapphire surface by high-energy X-ray reflectivity experiment.⁴²

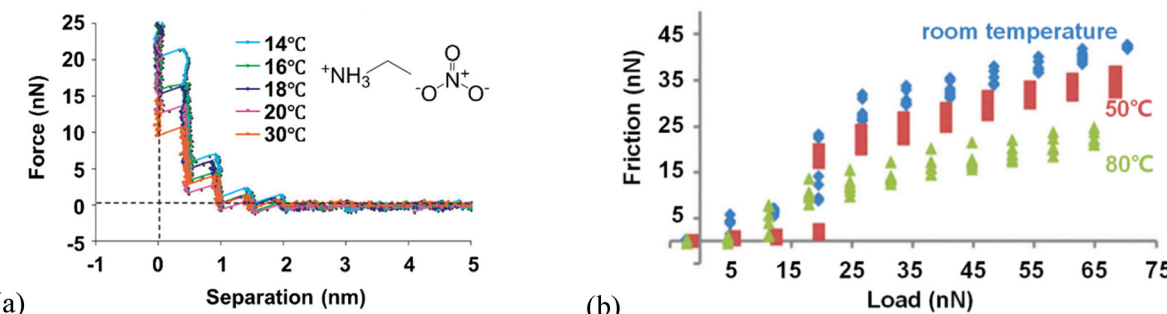


Fig. 11 (a) Force curves for an AFM Si₃N₄ probe approaching a mica surface in EAN at varying temperatures.⁴¹ Copyright 2010, Royal Society of Chemistry. (b) AFM friction loops at mica supported EAN surface with silica colloid probe at three different temperatures (scan velocity = 1 Hz).¹⁰² Copyright 2016, Royal Society of Chemistry.

In Fig. 11(b), the nanoscale friction force exhibits two distinct regimes at varying loads for EAN with a silica colloid probe on mica surfaces, confirming the robustness of the layering towards a temperature increase. The magnitude of the friction forces is much lower at higher temperatures, reflecting the lower dissipation forces, due to the decreased viscosity and increased thermal motion of ILs. Noting that in the high-load regime, the friction coefficients obtained from the slope of the linear region are almost temperature independent. That is because the density and conformation of the boundary layer in this regime are determined by the coulombic forces of ions with the surface and solvophobic interactions within the ion layers, which are not expected to change significantly as the temperature increases from room temperature to 80 °C.¹⁰² Except for the nanoscale friction, the slip length is also temperature-independent in EAN confined between mica and the silica colloid probe in this temperature range because of the unaffected boundary layer.

5.2. Surface charge and potential

When a solid surface meets an IL, molecular surface groups interact with the IL and form a chemical equilibrium defining the charge property of the IL–solid interface. The resulting different electrostatic properties determine the microstructures, interactions and the dynamics of ILs at interfaces.^{31,165–171} A solid surface can be charged in a liquid by either the ionization and/or dissociation of surface atoms or by the adsorption of ions from the solution onto the solid surface. ILs are more structured at highly charged surfaces than at neutral or nonpolar surfaces,^{41,56} for example, the structures of ILs in contact with a charged sapphire surface show a strong interfacial layering, starting with a cation layer at the surface and decaying exponentially into the bulk IL.⁴² Noting that the ion layering is completely different when the surface charges are buried by surface-functionalized groups. For example, the ILs [BMIM][BF₄] and [BMIM][PF₆] confined between negatively charged mica surfaces are found to exhibit molecular layering, strong viscosity enhancement, and eventually solid-like behavior. However, the same ILs, confined between methyl-terminated mica surfaces, do not display any pronounced layering and flow with their bulk viscosity.¹⁷² This is ascribed to the present charges on mica being buried on methyl-terminated surfaces, which determines the near-surface structure and dynamic properties of ILs.

The near-surface IL layers at charged solid interfaces can rearrange into more ordered layers reminiscent of lamellae, with the thickness consistent with the size of an ion pair.⁴⁴ Interestingly, an ordered ion structure was found to form near a neutral surface with a much lower diffusivity than the bulk, when the cation/anion of an IL is small and similar in size, *e.g.*, 1-ethyl-3-methylimidazolium bis(trifluoromethylsulfonyl) imide. However, an order-to-disorder transition in the ion structure occurs when the surface becomes charged, and this transition increases the interfacial diffusivity. In comparison, the structures of the ILs with a long nonpolar tail are disordered near both neutral and charged surfaces, so the surface

charge has relatively little impact on the diffusivity of these long-tailed ILs.¹⁷³

The potential-dependent structural layering of interfacial ILs can be well-observed using AFM under electrochemical control.¹⁴² Atkin's group examined the IL structuring at gold surfaces as a function of the surface potential using colloid probe AFM.¹³⁵ They found that as the surface potential increases, the ion layering of ILs at gold interfaces is more pronounced.¹³⁵ They also found the IL, 1-butyl-1-methylpyrrolidinium tris(pentafluoroethyl)trifluorophosphate, becomes more structured at the gold interfaces upon applying cathodic electrode potentials, in which both the number of ion layers and the force required to rupture these layers increase.³⁸ Fig. 12(a) shows typical force curves for an AFM probe approaching the Au(111) electrode in the neat IL 1-butyl-1-methylpyrrolidinium bis(trifluoromethylsulfonyl)amide ([Py₁₄][TFSA]), at three different surface potentials (OCP; +0.2 V; –0.2 V).¹⁷⁴ The observed steps at 0.6 nm, followed by 1.5, 2.4, and 3.3 nm, correspond to the rupturing of successive adjacent surface layers as the AFM probe approaches the gold surface. The forces required to rupture the layer adjacent to the electrode vary with the potential, which are 10, 6, and 3 nN, respectively, at –0.2 V, OCP, and +0.2 V. It is apparent that the near-surface multilayer structure of [Py₁₄][TFSA] with a more negative surface potential is relatively stronger. Noting that the rupturing force decreases for the layers further away from the Au electrode surface, indicating a weaker ordering of the layered structure away from the surface. In the work by Atkin *et al.*, they also observed different multiple ion layers in the ILs (1-ethyl-3-methylimidazolium bis[(trifluoromethylsulfonyl)]amide ([EMIM][TFSA]) and 1-butyl-1-methylpyrrolidinium bis[(trifluoromethyl)-sulfonyl]amide ([BMP][TFSA])) as a function of the surface potential at gold surfaces.¹⁷⁵ At a higher surface potential, the longer-chained [BMP]⁺ interacts more strongly with the gold surface than the shorter-chained [EMIM][TFSA], requiring a greater force to rupture the ion layer in [BMP][TFSA] and leading to a more structured ion layer.

Fig. 12(b) shows that the composition in the confined ion layer of the IL, 1-butyl-1-methylpyrrolidinium tris(pentafluoroethyl) trifluorophosphate ([Py₁₄][FAP]) between the silica colloid probe and the Au(111) surfaces, changed from the cation-enriched at negative potentials to anion-enriched at positive potentials. These different ion layers at interfaces result in the potential-controlled friction,^{177,178} in which the friction force of the IL decreases as the electrical potential varies from positive to negative.³³ One possible explanation for the decreased friction at the negative surface potential is the more lubricating alkyl tails of cations,³³ and the strong electrostatic attraction of cations to the surface hinders the squeeze-out of the IL,^{146,179} preventing stiction and allowing the layers to slide easily over one another. However, the potential-dependent friction in the other IL, 1-hexyl-3-methylimidazolium tris (pentafluoroethyl)trifluorophosphate ([HMIM][FAP]) confined between a sharp silica AFM probe and a graphite surface exhibited an opposite trend (Fig. 12c). The friction force and friction coefficient μ obtained at positive potentials are lower

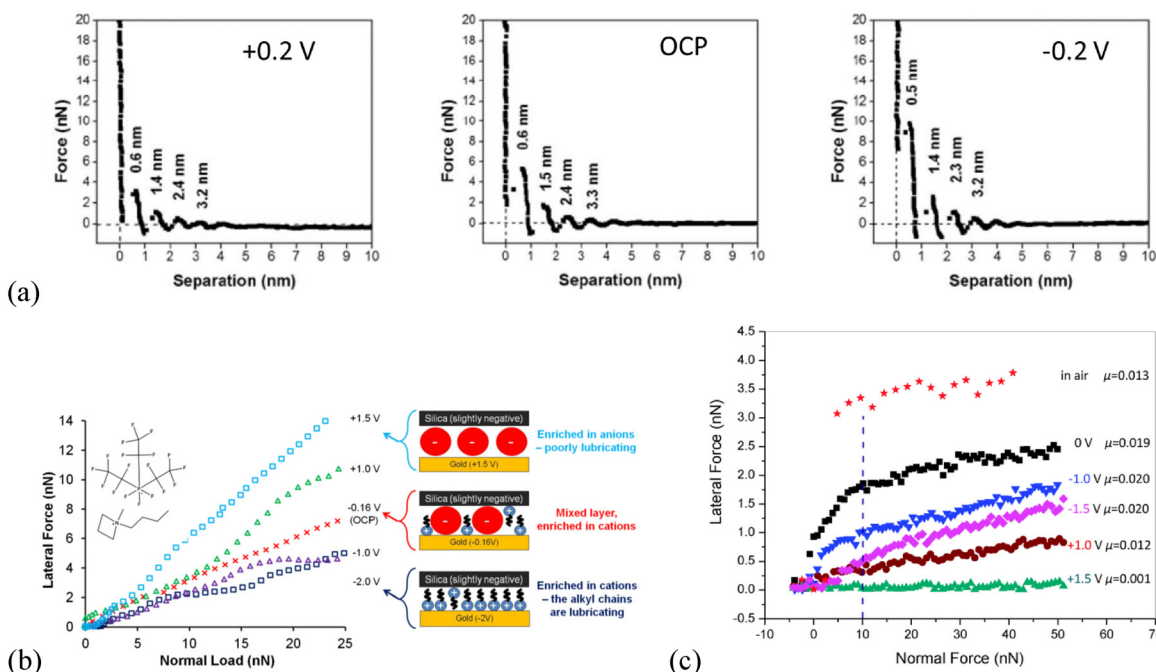


Fig. 12 (a) Typical force curves for an AFM probe approaching the Au(111) surface in the neat IL $[\text{Py}_{14}]\text{[TFSA]}$ at different electrode potentials (OCP, +0.2 V and -0.2 V). OCP = open circuit potential.¹⁷⁴ Copyright 2018, Royal Society of Chemistry. Lateral force versus normal load for different surface potentials for (b) $[\text{Py}_{14}]\text{[FAP]}$ confined between a silica colloid probe and the Au(111) electrode surface,³³ Copyright 2012, American Physical Society. (c) $[\text{HMIM}]\text{[FAP]}$ confined between a sharp silica probe and graphite surface.¹⁷⁶ Copyright 2014, Royal Society of Chemistry.

than those at negative ones. This is so-called switched on/off electrolubrication¹⁸⁰ of confined ILs by polarizing the surface relative to the reference electrode.¹⁷⁶ Particularly at a positive potential of +1.5 V, the friction coefficient falls to an ultra-low level, in which, $\mu = 0.001$, much less than 0.01, defining super-lubricity (Fig. 12c). Most of the cations have been expelled on the surface with a biased voltage of +1.5 V, leaving a smooth and highly anion-enriched interfacial layer. With the absence of the cation reorientation, the energy dissipation due to local stick-slip events is minimal, resulting in an ultra-low friction coefficient consistent with super-lubrication.¹⁷⁶

5.3. Load

One important milestone of friction mechanism was established in the 17th century^{95–97} that friction force is linearly proportional to the normal load. This theorem is also known as Amontons' Law, in which the monotonic increase of friction with load has been observed across a range of length scales,⁹⁹ as described in section 2.2. While an AFM study of non-halogenated phosphonium-based ILs/glycol ether mixtures at titanium interfaces reveals a negative load-dependence, *i.e.*, the friction force decreases as the normal load increases (Fig. 13a). The structural reorientation of these studied ILs is responsible for this observed negative load-dependent friction, in which, as the normal load increases, the cation alkyl chains prefer to show parallel orientation to the probe scanning path. The parallel-oriented ion structures, similar to the 'blooming lotus leaf', produce a new sliding interface and reduce the friction

force.²⁸ Such a negative correlation between friction force and normal load is not inherent in the Amontons's law. Yet, it has been observed from various systems (*e.g.*, graphite, graphene, polymers, or other two-dimensional materials,) and under different conditions (such as a vacuum).^{107–112}

Rutland's group¹⁰² observed two distinct friction regimes at varying loads for EAN with silica colloid probes on mica surfaces, as shown in Fig. 13(b). The absolute friction force is considerably larger in the high load region (>20 nN) than in the low load region (<15 nN). Apparently, the probe shears against the less ordered ion structure of the ILs at low loads, while against the highly ordered ILs on the surface at high loads. As shown in Fig. 13(c), a series of force-measurements with increasing normal loads of 500 pN–18 nN are performed to examine the ion layering as the probe approaches the surface.¹⁸¹ During the measurements, the layered ion structures of the IL 1-ethyl-3-methylimidazolium bis(trifluoromethylsulfonyl) imide $[\text{EMIM}]\text{[Tf}_2\text{N}]$ can be clearly observed. For example, at a low normal load F_N of 500 pN, only 3 ion layers appear (layer 3 to 5), while 4 layers are observed at 1 nN (layer 2 to 5). No additional ion layers are observed with increasing normal load at a normal load of 14 nN, because a further increase of the normal load to 18 nN does not reveal further ion layers, indicating that a normal load of 14 nN is enough to puncture all ion layers at $[\text{EMIM}]\text{[Tf}_2\text{N}]$ -mica interfaces. The increase in the normal load is coupled with a distinct increase in the adhesion force derived from the retraction curve.

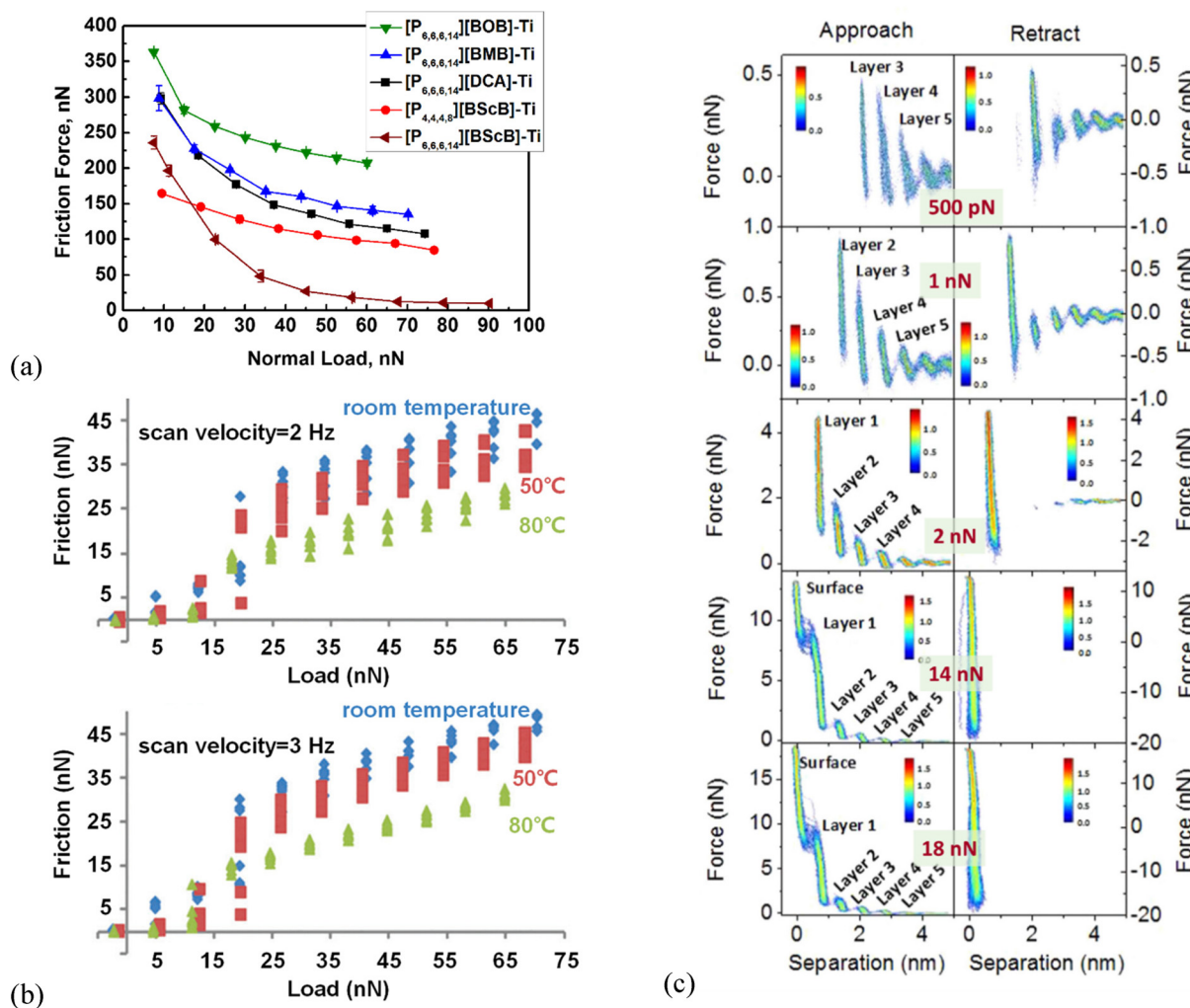


Fig. 13 (a) Friction measurements for the IL/oil mixtures coated Ti interfaces at varying loads, where 75 wt% of ILs were added into the base oil diethylene glycol dibutyl ether. The studied ILs are non-halogenated phosphonium based ILs, i.e., trihexyltetradecylphosphonium bis(oxalato)borate, $[P_{6,6,6,14}][BOB]$; trihexyltetradecylphosphonium bis(mandelato)borate, $[P_{6,6,6,14}][BMB]$; trihexyltetradecylphosphonium dicyanamide, $[P_{6,6,6,14}][DCA]$; tributyoctylphosphonium bis(salicylate)borate, $[P_{4,4,4,8}][BScB]$; trihexyltetradecylphosphonium bis(salicylato)borate, $[P_{6,6,6,14}][BScB]$.²⁸ Copyright 2018, Wiley-VCH. (b) AFM friction loops at mica supported EAN surface with silica colloid probe at varying temperatures (top: scan velocity = 2 Hz, bottom: scan velocity = 3 Hz).¹⁰² Copyright 2016, Royal Society of Chemistry. (c) 2D histograms of approach (left) and retract (right) portion of 50 measured force curves in $[EMIM][Tf_2N]$ on mica with increasing normal load (F_N) of 500 pN, 1 nN, 2 nN, 14 nN, and 18 nN, respectively. The color bar represents the common logarithm of the frequency of data points in each bin.¹⁸¹ Copyright 2016, Springer Nature.

5.4. Humidity

Tuning the microstructure and ILs layering at solid interfaces offers leverage to tailor the performance of ILs in applications such as batteries, super-capacitors, lubrication and so on.^{8,182,183} In IL-based supercapacitors and electrocatalysis, small amounts of absorbed water are found to reduce the electrochemical window and cause performance degradation.¹⁸⁴ Trace water can significantly impact near-surface IL structures,^{22,133,184–186} by either enhancing or disrupting bound ion layers,^{87,89,147,182} which depends on the relative strength of ion-surface and water-surface interactions.^{56,87} For example, adsorbed water appears to alter the ion-pair orientation and charging characteristics to prevent the liquid-to-

solid transition of ILs, and so on;^{34,86,89,147} in the presence of trace amounts of water, the IL, 1-hexyl-3-methylimidazolium ethylsulfate, at the mica interface, reveals an additional ion layer;⁸⁶ while in some humid cases, the IL layering can be disrupted due to both packing and capillary effects, above a certain water threshold.^{86,89,147}

On the other hand, the layered ion structures of ILs at solid interfaces can be altered by adding trace water, and with the increase of water concentration, the long-range monotonic force of ILs at solid interfaces switches from van der Waals attraction to double layer repulsion.¹⁸⁷ In the context of the interfacial structuring of ILs, the effects of water strongly depend on both surface charging and interfacial wetting properties. In general, the effect of water on IL structuring is a

consequence of balances between ion–water, ion–surface, surface–water, and surface–ion interactions that may vary greatly at different ion/solid interfaces.⁸⁹ A significant evolving influence of water on the interfacial IL layering is observed by silica-coated silicon AFM probes (probe radius ~10 nm) in Fig. 14(a). The dynamic evolution of the force curves at the IL/mica interfaces over about 6 hours after solvation with humid and dry IL, [1-ethyl-3-methylimidazolium][bis(trifluorosulfonyl)imide], i.e.,[C₂mim][Tf₂N] is respectively shown in the left and middle panels in Fig. 14(a). Immersing mica in the humid [C₂mim][Tf₂N] for 46 min, two prominent ion layer populations appear at ~22.6 and 29.8 Å away from the hard mica surface. After longer exposure to the humid IL, additional prominent populations with increasing resistance to squeeze-out appear at shorter separation distances. The increasing slope of the layering forces in the force curves reflects an increase in ions packing density, which results in a harder ion structure. In comparison, the layering at dry IL/mica interfaces is weaker and broadly distributed, only extending over about three layers into the bulk. The right panel in Fig. 14(a) records the corresponding adhesion force, which gradually increases by a factor of about two over time in the humid case, due to the strong interfacial layering. The initial stronger attractive force in the humid IL than in the dry one is attributed to the interfacial hydration of

water molecules, leading to the K⁺ dissolution of the mica substrate and consecutive strong ion layering. While how exactly the water is incorporated into the remaining layer remains elusive.⁸⁹

Recently, Fajardo *et al.* concluded that the presence of water in IL lubricants is rather a foe.¹⁸⁵ They found in small amounts, water increases friction, although at larger amounts this trend slightly reverses (Fig. 14b). The water adsorption increases the friction force, because it screens the electrostatic interactions between the ions, making the IL lubricant more “fluid” and compressible and hence less resistant to an external load. The more compressible behavior of ion layers due to the existence of water is also confirmed at 1-butyl-1-methylpyrrolidinium bis(trifluoromethylsulfonyl)amide ([BMP][TFSA])-Au(111) interface,¹⁸⁸ in which the stiffness of the first ion layers decreases significantly upon the water increase from 30 to 90 ppm (Fig. 14c). The decreased stiffness demonstrates that water molecules in the electric double layer have weakened the interactions between cations, anions, and the surface. In addition, for each water concentration, a more negative potential results in a smaller stiffness of the first ion layer, while this stiffness change with potential becomes smaller as the water concentration increases.

The confined IL films are often determined to be solid-like, and the addition of water is to enhance the structure of the IL,

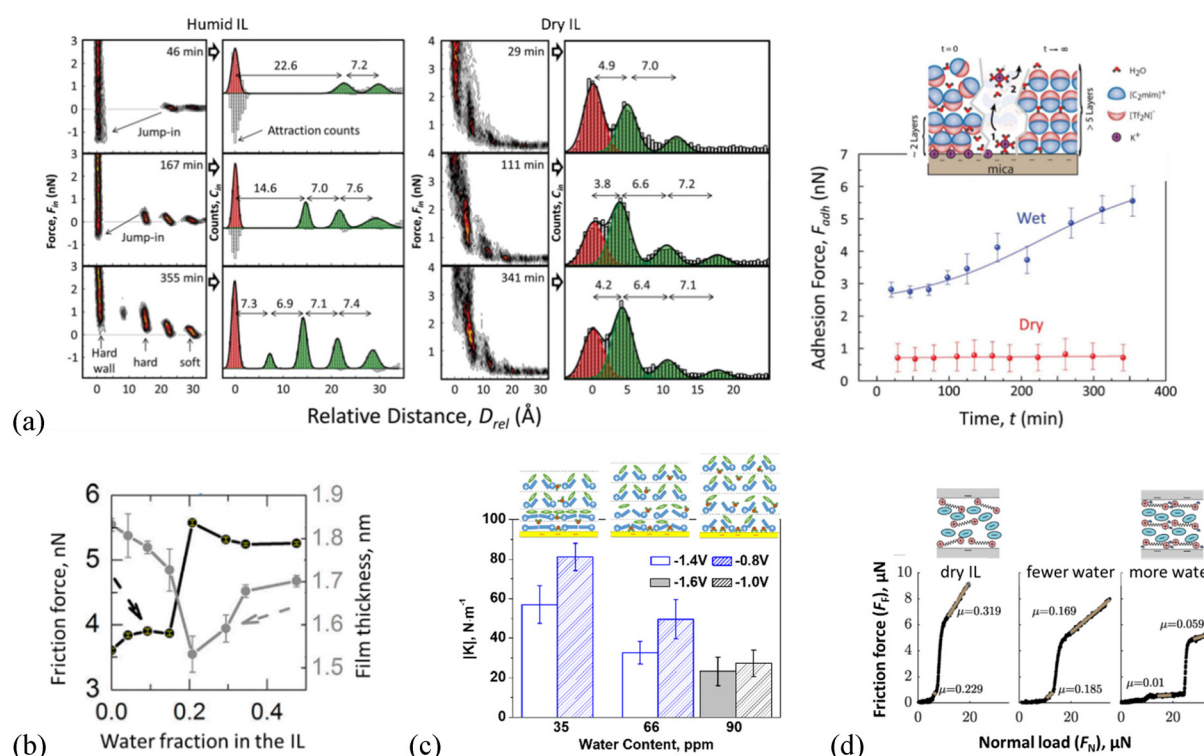


Fig. 14 (a) Left and middle: interfacial ion layering characteristic of humid and dry IL [C₂mim][Tf₂N] over ~6 h; right: time evolution of the adhesion forces of silica probes in humid and dry IL on mica, and the inset is the schematic interpretation of the observed surface charging and layering on mica surfaces in the humid IL.⁸⁹ Copyright 2015, Wiley-VCH. (b) Impact of hydration of the nanoscale IL film on the lubrication.¹⁸⁵ Copyright 2017, American Chemical Society. (c) The stiffness | K | of the first layer of [BMP][TFSA] at Au(111) with different amounts of water under different potentials.¹⁸⁸ Copyright 2016, Wiley-VCH. (d) Friction force as a function of normal load, for the dry IL as well as the ILs with few and more water.¹⁴⁹ Copyright 2019, American Chemical Society.

leading to increased activation barriers and more strongly corrugated energy landscape, which are expected to increase the friction coefficient. However, the friction coefficient of the dicationic IL, 1,10-bis(3-methylimidazolium)decane di[bis(trifluoromethylsulfonyl)-imide] confined between mica surfaces decreases with increasing water content (Fig. 14d).¹⁴⁹ The friction force exhibits discontinuities as the IL layers are squeezed out at a higher normal load. The resulting friction coefficient is observed to be more than an order of magnitude lower than for the dry IL at the same value of normal load. This observation is particularly notable for its contrast with several previous cases, where water tended to increase friction. The confined dicationic IL herein is different from the normal ILs, in which the striking enhancement of lubrication effect with the incorporation of water is probably due to more well-defined ion layers in the z-direction, creating low-stress planes for shearing.¹⁴⁹

5.5. Velocity

The variation of friction with velocity is dependent on the applied normal load.^{179,189} The friction force of an IL, 1-ethyl-3-methyl imidazolium bis-(trifluoro-methylsulfonyl) imide on a mica surface, varies non-monotonically with the sliding velocity of silica colloid AFM probe (~5 µm diameter), in which it slightly decreases with velocity and then rapidly increases above a transition velocity v^* (Fig. 15a).¹⁹⁰ This non-monotonic dependence of the friction with velocity not only occurs in this system but also appears for other ILs¹⁴⁷ and lubricants.¹⁹¹ For example, the friction decreases with the increasing velocity under a high normal load (30.4 nN), while increases with the increasing velocity under a low normal load (3.8 nN), for a silicon AFM probe immersed in an IL [EMIM][TFSI], sliding against a silicon (100) wafer.

In contrast, a monotonic velocity dependence on nanofriction is also observed at IL-solid interfaces, *e.g.*, the friction forces and corresponding friction coefficient are smaller at lower sliding velocity for EAN on mica with a silica colloid AFM probe (~20.8 µm diameter, Fig. 15b). The friction force increases with the normal load over the full range of sliding velocity examined, being consistent with the results shown in Fig. 15(a). Compared with the normal approaching force curve shown on a common load abscissa in Fig. 15(b), the friction response can be decomposed into 3 linear regions (interval I, II, and III) with distinct slopes as the corresponding friction coefficient. At small normal loads (I), there are 4 ion pair layers of EAN between the silica probe and mica, and the velocity-independent friction increases relatively steeply with the normal load. At intermediate loads (II), the friction coefficient increases logarithmically with the sliding velocity, and the force curve reveals a single confined layer of cations remaining between the surfaces. At high loads (III), the friction coefficient is small and once again, independent of sliding velocity. For the interval III, the ion layer is compressed by the high load and bound primarily to the mica substrate to form a well-defined sliding plane, allowing the silica probe to slide easily.¹⁸⁹

Atkin's group investigated the effect of sliding velocity on the friction as a function of potential in the IL, 1-ethyl-3-methylimidazolium tris(pentafluoroethyl)trifluorophosphate, [EMIM][FAP] at Au(111) surfaces, with silica colloid probes (~5 µm diameter). They found the velocity effect of the IL on nanofriction is pronounced at neutral Au(111) surfaces, in which the friction force increases with sliding velocity for a given normal load (left panel, Fig. 15c). However, this effect on the IL nanofriction is relatively weak when the surface is charged (potential of -2.0 V and +1.5 V, middle and right panels, Fig. 15c), because the oppositely charged ions are strongly bound to the surface to form a relatively rigid, ordered layer.⁵³ The weakened velocity effect on charged surfaces agrees with the velocity-independent friction observed previously in the SFA measurements for the IL 1-ethyl-3-methyl imidazolium ethylsulfate, [EMIM][EtSO₄] confined between two negatively charged mica sheets, which is due to the formed solid-like IL film.¹⁴⁷ The dependence of the slip length of the IL [HMIM][TFSI] on the sliding velocity is similar at varying roughness, in which the slip length increases as the velocity increases, as shown in the right panel in Fig. 15(d). Compared with the lower and higher roughness of the surfaces (RMS = 0.1, 6 nm), a maximum slip length of the IL is observed on the surface with an intermediate surface roughness (RMS = 4.9 nm), and the roughness effect on the velocity-dependent slip length is more significant in this case.¹²⁶

5.6. Mixture of ILs and molecular liquids

Molecular liquids and nano-object additives have proven to be significant in macro-, micro-, and nanoscale studies, influencing the interaction forces and microstructure¹⁹² of ILs at solid interfaces. As shown in Fig. 16(a), the force profiles of various EAN–water mixtures at silica surfaces for the approach of a 4.8 µm glass colloid probe exhibit a strong water-dependence.¹⁹³ The electrostatic repulsion dominates in the neat water, while at the highest concentration of water (95 wt%) in EAN, an attractive dispersion force produces a jump into contact from 5 nm separation. The attractive force decreases as the water concentration decreases to 50 wt%, due to the reduction in the Hamaker constant, which is much smaller in the neat EAN than water. The layering structure appears when the water concentration decreases to 25 wt% with an EAN concentration of 75 wt%, while the ion layering is apparent at an EAN–water mixture with 10 wt% water, and no attractive forces are observed. The force required to rupture the innermost ion layer is much higher in the neat EAN than the EAN with 10 wt% water, indicating that the addition of water reduces both the number and resilience of EAN ion layers. Steps in the force profile are also noted upon retraction especially in the neat EAN, due to the layer reformation.

The nanofrictional behavior of ILs can be significantly influenced by the addition of base oil because of the differing ion structures at interfaces.^{28,194} For example, adding base oil into non-halogenated phosphonium-based ILs with molar ratios of 1 : 70, 1 : 10, and 1 : 1 (IL : oil) results in completely

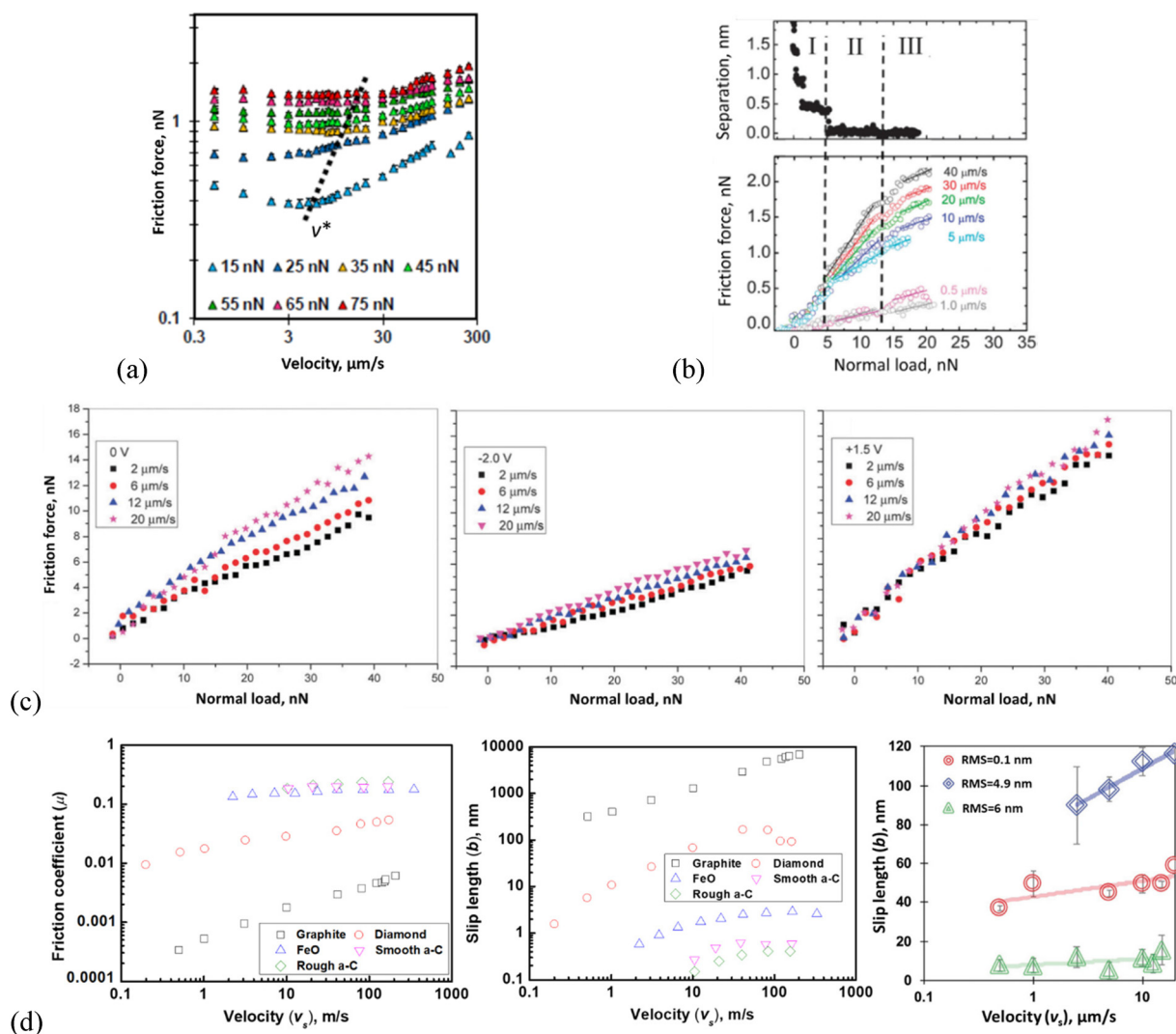


Fig. 15 (a) Speed-dependent friction force measured in an IL, 1-ethyl-3-methyl imidazolium bis-(trifluoro-methylsulfonyl) imide on a mica surface.¹⁹⁰ Copyright 2018, MDPI. (b) At EAN–mica interfaces, top: force versus separation; bottom: friction force measurements for various sliding velocities versus normal load. Solid lines denote linear fits to increasing load data from which friction coefficients are obtained.¹⁸⁹ Copyright 2012, Royal Society of Chemistry. (c) Friction force vs. normal load at different sliding velocities for [EMIM][FAP] on Au(111), left: 0 V, middle: -2.0 V, right: +1.5 V.⁵³ Copyright 2013, Royal Society of Chemistry. Silica colloid AFM probes are used in (a)–(c). (d) Friction coefficient (left) and slip length (middle) variations with the sliding velocity, for the IL, 1,3-dimethylimidazolium bis(trifluoromethylsulfonyl)imide [mmlm][NTf₂] confined between graphite surfaces.¹³¹ Copyright 2018, American Chemical Society. The right panel is the slip length variation of the IL 1-hexyl-3-methylimidazolium bis(trifluoromethylsulfonyl) imide ([HMIM][TFSI]) with the sliding velocity at differently nano-roughened silicon surfaces, using the silicon probe. RMS represents the root mean square roughness.¹²⁶ Copyright 2020, Wiley-VCH.

different friction behavior at Ti surfaces. In the case of the $[P_{6,6,6,14}][BScB]$ -oil mixture (Fig. 16b, left),¹⁹⁴ a significant reduction is observed in the friction coefficient μ for the mixture with a higher IL concentration (1 : 10, $\mu \sim 0.056$), compared with that for the lower IL concentration 1 : 70 ($\mu \sim 0.100$). At a higher IL concentration, the IL prefers to accumulate at the surface, forming an *IL-rich* layered structure. The *IL-rich* layered structure consists of two parts: (1) the IL adjacent to the surface arranging in ordered layers (dense layer, t_{LD}), and (2) the upper IL with decayed ordering into layers at a greater distance from the surface (loose layer, t_{LL}). These ordered *IL-rich* layers formed on the Ti surface facilitate the

reduction of the nanoscale friction by preventing direct surface-to-surface contact. However, the ordered IL layers disappear in the case of a lower IL concentration (1 : 70), resulting in incomplete boundary layers, because the ions are displaced by oil molecules during the sliding, being less efficient in the friction reduction. The upper loose IL layer is less stable, through which the escape of the ions might occur, and the existing oil on the top at a greater distance to the substrate blocks this escape. Thus, a further increase of the IL concentration will not necessarily bring a smaller friction coefficient, because it results in a smaller fraction of the oil, which cannot ensure the block of the ion escape. In the case of the IL-oil

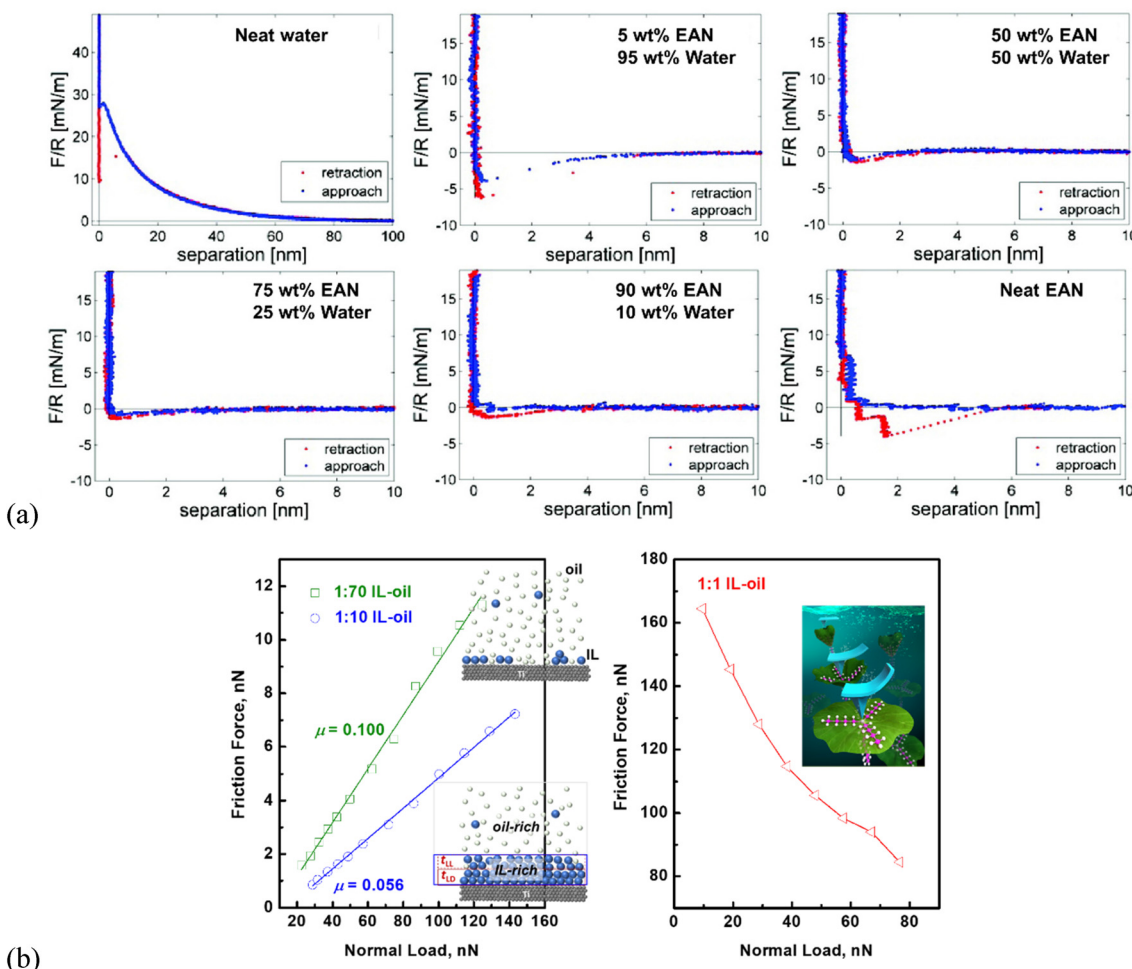


Fig. 16 (a) Force curves for the approach and retraction of a $4.8\text{ }\mu\text{m}$ colloid probe to a silica surface immersed in EAN–water mixtures with varying water concentrations (100 wt%–0 wt%) at $21\text{ }^\circ\text{C}$.¹⁹³ Copyright 2010, American Chemical Society. (b) Friction force measurements in IL–oil mixtures at Ti surfaces with Si_3N_4 AFM probes.^{28,194} Copyright 2018, Wiley-VCH. Copyright 2022, Springer Nature. The IL is trihexyltetradecylphosphonium bis (salicylato)borate ([P_{6,6,6,14}][BScB]) and the oil is diethylene glycol dibutyl ether.

mixtures with a molar ratio of $\sim 1:1$ (Fig. 16b, right), the magnitude of the measured friction forces is much higher than that in the case of dilute solutions with molar ratios of $1:70$ and $1:10$. A negative load-dependent friction behavior, where the friction decreases as the normal load increases, not following Amontons' law, is attributed to the structural reorientation of the ILs.²⁸

It has been reported that the frictional performance may not necessarily be improved by a higher concentration of ILs.⁵⁷ At the nanoscale, 98 mol% hexadecane with only 2 mol% IL trihexyl(tetradecyl)phosphonium bis(2,4,4-trimethylpentyl) phosphinate enables a significant reduction in the friction force by forming robust boundary layers.¹⁹⁵ In another study, the friction was found to be reduced effectively with 1 wt% quaternary ammonium IL in poly- α -olefin oil, while a further increase of the IL from 1 to 3 wt% does not make any significant changes in this friction-reducing characteristic.¹⁹⁶ 8 wt% imidazolium-based ILs in glycerol show a higher friction coefficient at steel–steel contacts than that of 0.63 wt%.¹⁹⁷

While in the rapeseed oil lubrication, the friction coefficient increases as the IL concentration increases from 1 to 3 wt%.¹⁹⁸

6. Conclusions and outlook

AFM has been successfully used to probe the interactions and microstructures of ILs at solid interfaces and their interplay, directing the tailoring of the heterogeneity of solid surfaces, the nature of ILs, and the surrounding condition, to manipulate the function of ILs and even affect the magnitude. Our understanding of the interactions and microstructures of ILs at solid interfaces has advanced considerably *via* AFM-measured force curves, friction force and slip length in the past few years. A host of IL-based applications such as super-lubricity^{6,7} and high energy density electrolyte,^{8–15} have been demonstrated to be strongly correlated to the interactions and microstructures of near-surface ILs.

Despite great progress in the fundamental understanding of the interactions and ion structuring of ILs at solid interfaces through AFM, there are still several emerging challenges and opportunities for both the scientific community and engineers, and some of them are highlighted as follows.

(1) *In situ observations of interaction–microstructure changes at IL–solid interfaces:* The IL–solid interface scanned via AFM can be regarded as a complex “black box” composed of an AFM probe, ILs, and solid surfaces with characteristic roughness, chemistry and charges. One question arises: how can one detect the simultaneous interaction–microstructure changes of ILs occurring at IL–solid interfaces? The combination of AFM and some other advanced techniques will enable our deeper exploration of IL behavior at solid interfaces. For example, *in situ* AFM and ultra-small-angle X-ray scattering have been coupled to study the evolution of electrode morphology in an imidazolium based IL electrolyte.¹⁹⁹ *In situ* AFM-electrochemical measurements have made a direct observation of the transition from a multilayered structure to a double-layer structure of the ILs at gold electrodes.¹³³ Three-dimensional AFM has been developed to map the solid–liquid interfaces,^{200–203} which might be jointly used with AFM force measurements to probe the *in situ* changes of the interactions and microstructures of ILs at solid interfaces. The potential-dependent double layer structure of IL ions at the interface has been monitored within the electrochemical window using *in situ* IR-visible sum-frequency generation spectroscopy.²⁰⁴ *In situ*, real-time IR measurements during potential scans have enabled the probing of the reorientation of IL ions at the electrode interface simultaneously.²⁰⁵ *In situ* AFM and Raman spectroelectrochemistry have been used to detect the electrochemically induced phase separation process that starts in the IL electrolyte near the electrode surface. Integrating these advanced spectroscopic techniques with AFM,²⁰⁶ will make it possible to quantitatively analyze the interfacial contributions to the IL behavior and realize *in situ* observations of interaction–microstructure changes at IL–solid interfaces.

(2) *Quantitative model for predicting IL behavior at solid interfaces:* A lack of direct quantitative linking the strength of ILs–solid interactions to its properties, from both experimental and theoretical points of view, has prevented a complete understanding of the mechanism in the applications of ILs. There is an urgent need for quantitative modeling to provide rational guidance for designing IL-based applications. AFM bridges atomic-scale physics and the nanoscale behavior, and we believe AFM probing and uncovering the intrinsic mechanism behind IL–solid interfacial phenomena would provide an effective way to quantitatively describe and predict the IL behavior at heterogeneous solid interfaces. The earlier AFM exploration of molecular liquid behavior on planar solid surfaces obtained a quantitative interplay between nanofriction at liquid–solid interfaces and molecular interactions.¹¹⁷ This indicates that it is possible to achieve the quantitative linking of ILs–solid interactions to their properties at heterogeneous solid interfaces through AFM, which opens up an opportunity

for quantifying and predicting IL behavior on solid surfaces at the molecular level.

(3) *Screening IL–solid interfaces for targeted properties:* Considering the nearly immeasurable large number of potential ILs, various solid surfaces, and complicated environmental conditions,²¹ it is challenging to identify the proper ILs for specific solid interfaces with targeted properties and performance. Theoretical studies, such as coarse-grain (CG) molecular dynamics simulations, are highly useful for the effective development of design and applications²⁰⁷ from the IL–solid systems. However, a tedious parametrization of the CG interactions and their verification are needed in advance, while obtaining reliable force field and interaction parameters, and any attempts to develop them are very difficult without accurate experimental data.^{208,209} The quantified molecular interaction between one single IL molecule with the overall solid surface makes it possible to offer the needed information to derive interaction parameters in the CG force field. AFM experiments so far have dealt with the overall force of ensembles of atoms or molecules, because the interaction taking place in real systems is an integration over the volumes of the interacting molecules, rather than the simple summation of coupling of individual molecules contributions.²¹⁰ The difficulty is to isolate the interaction of one single IL molecule with the solid surface directly from AFM force curves,²¹¹ which are affected by surface heterogeneities, IL nature and the surrounding conditions. A colloid probe AFM-based methodology²¹² was proposed to quantify the molecular interaction forces between a single IL molecule and charged SiO₂ surfaces.²¹³ While the applicability and reliability of these obtained molecular interactions to derive the interaction parameters in the CG force field is not clear.

Therefore, looking toward the future, it is important to continue developing new AFM-based advanced techniques and to obtain a quantitative understanding of the interactions and microstructures of ILs at solid interfaces in a controllable manner.

Abbreviations

[BMIM][PF ₆]	1-Butyl-3-methylimidazolium hexafluorophosphate
[C ₃ mpyr][FSI]	N-Methyl-N-propylpyrrolidinium bis(fluorosulfonyl)imide
EAN	Ethylammonium nitrate
[P _{6,6,6,14}] ⁱ [(C ₈) ₂ PO ₂]	Trihexyl(tetradecyl)phosphonium bis(2,4,4-trimethylpentyl)-phosphinate
[C ₅ Py][NTf ₂]	1-Pentylpyridinium bis(trifluoromethane-sulfonyl) imide
[P _{6,6,6,14}][BMB]	Trihexyltetradecylphosphonium bis(mandelato)borate
PC	Propylene carbonate
[EMIM][TFSI]	1-Ethyl-3-methylimidazolium bis(trifluoromethylsulfonyl)imide
PAN	Propylammonium nitrate

[HMIM][TFSI]	1-Hexyl-3-methyl imidazolium bis(trifluoromethylsulfonyl)imide	[P _{6,6,6,14}][BScB]	Trihexyltetradecylphosphonium bis(salicylato)borate
[Emim][Tf ₂ N]	1-Ethyl-3methyl-imidazolium bis(trifluoromethanesulfonyl) imide	[C ₂ mim][Tf ₂ N]	[1-Ethyl-3-methylimidazolium][bis(trifluorosulfonyl)imide]
[Emim][Tfo]	1-Ethyl-3-methylimidazolium trifluoromethyl-sulfonate	[EMIM][EtSO ₄]	1-Ethyl-3-methyl imidazolium ethylsulfate
[HMIM][FAP]	1-Hexyl-3-methylimidazolium tris(pentafluoroethyl)tri-fluorophosphate	[mmIm][NTf ₂]	1,3-Dimethylimidazolium bis(trifluoromethylsulfonyl)imide
[EMIM][FAP]	1-Ethyl-3-methylimidazolium tris(pentafluoroethyl)tri-fluorophosphate		
[EMIM][TFSA]	1-Ethyl-3-methylimidazolium bis(trifluoromethylsulfonyl)imide		
[BMIM][FAP]	1-Butyl-3-methylimidazolium tris(pentafluoroethyl)-Trifluorophosphate		
EtAN	Ethanolammonium nitrate		
EAFF	Ethylammonium formate		
PAF	Propylammonium formate		
EMAF	Ethylmethylammonium formate		
DMEAFF	Dimethylethylammonium formate		
Li(G3)TFSI	Lithium triglyme bis(trifluoromethylsulfonyl)imide		
Li(G4)TFSI	Lithium tetraglyme bis(trifluoromethylsulfonyl)imide		
Li(G4)BETI	Lithium tetraglyme bis(perfluoroethylsulfonyl)imide		
Li(G3)TFA	Lithium triglyme trifluoroacetate		
Li(G1)2TFSI	Lithium di-monoglyme bis(trifluoromethylsulfonyl)imide		
[P _{6,6,6,14}][TFSI]	Trihexyl-(tetradecyl)phosphonium bis(trifluoromethane)sulfonamide		
[P _{4,4,4,1}][TFSI]	Tributyl-(methyl)phosphonium bis(trifluoromethane)sulfonamide		
[C ₄ C ₁ Im][AOT]	1-Butyl-3-methylimidazolium 1,4-bis(2-ethylhexoxy)-1,4-dioxobutane-2-sulfonate		
[C ₄ C ₁ Im][BF ₄]	1-Butyl-3-methylimidazolium tetrafluoroborate		
[C _n MIM][BF ₄]	1-n,2-Methylimidazolium tetrafluoroborate ($n = 2, 4, 6$)		
[HOC ₄ Py][NTf ₂]	1-(4-Hydroxybutyl)pyridinium bis(trifluoromethanesulfonyl)imide		
[BMIM][BF ₄]	1-Butyl-3-methylimidazolium tetrafluoroborate		
[HMIM][NTf ₂]	1-Hexyl-3-methylimidazolium bis(trifluoromethylsulfonyl)imide	bis	
[Py ₁₄][TFSA]	1-Butyl-1-methylpyrrolidinium (trifluoromethylsulfonyl)amide	bis	
[BMP][TFSA]	1-Butyl-1-methylpyrrolidinium bis[(trifluoromethyl)-sulfonyl]amide	bis	
[P _{6,6,6,14}][BOB]	Trihexyltetradecylphosphonium bis(oxalato)borate	bis	
[P _{6,6,6,14}][BMB]	Trihexyltetradecylphosphonium bis(mandelato)borate		
[P _{6,6,6,14}][DCA]	Trihexyltetradecylphosphonium dicyanamide		
[P _{4,4,4,8}][BScB]	Tributyoctylphosphonium bis(salicylate) borate		

Conflicts of interest

The authors declare no conflict of interest.

Acknowledgements

The authors are grateful for the funding from the Natural Science Foundation of Jiangsu Province (Grant No. BK20191289) and the National Natural Science Foundation of China (Grant No. 21978134, 21838004, and 21878144). X. Ji thanks the financial support from the Swedish Research Council. A. Laaksonen acknowledges the Swedish Research Council for financial support, and partial support from a grant from Ministry of Research and Innovation of Romania (CNCS – UEFISCDI, Grant No. PN-III-P4-ID-PCCF-2016-0050, within PNCDI III). F. U. Shah gratefully acknowledges the financial support from the Swedish Research Council (Grant No. 2018-04133).

References

- 1 J.-K. Kim, A. Matic, J.-H. Ahn and P. Jacobsson, *J. Power Sources*, 2010, **195**, 7639–7643.
- 2 N. Karimi, M. Zarzabeitia, A. Mariani, D. Gatti, A. Varzi and S. Passerini, *Adv. Energy Mater.*, 2021, **11**, 2003521.
- 3 J. Feng, Y. Wang, Y. Xu, Y. Sun, Y. Tang and X. Yan, *Energy Environ. Sci.*, 2021, **14**, 2859–2882.
- 4 M. Kar, Z. Ma, L. M. Azofra, K. Chen, M. Forsyth and D. R. MacFarlane, *Chem. Commun.*, 2016, **52**, 4033–4036.
- 5 S. Zhang, J. Zhang, Y. Zhang and Y. Deng, *Chem. Rev.*, 2017, **117**, 6755–6833.
- 6 M. Cai, Q. Yu, W. Liu and F. Zhou, *Chem. Soc. Rev.*, 2020, **49**, 7753–7818.
- 7 F. Zhou, Y. Liang and W. Liu, *Chem. Soc. Rev.*, 2009, **38**, 2590–2599.
- 8 X. Mao, P. Brown, C. Červinka, G. Hazell, H. Li, Y. Ren, D. Chen, R. Atkin, J. Eastoe, I. Grillo, A. A. H. Padua, M. F. Costa Gomes and T. A. Hatton, *Nat. Mater.*, 2019, **18**, 1350–1357.
- 9 D. A. Rakov, F. Chen, S. A. Ferdousi, H. Li, T. Pathirana, A. N. Simonov, P. C. Howlett, R. Atkin and M. Forsyth, *Nat. Mater.*, 2020, **19**, 1096–1101.
- 10 A. Eftekhari, *Energy Storage Mater.*, 2017, **9**, 47–69.
- 11 K. L. Van Aken, M. Beidaghi and Y. Gogotsi, *Angew. Chem., Int. Ed.*, 2015, **54**, 4806–4809.

- 12 P. F. R. Ortega, G. A. dos Santos, J. P. C. Trigueiro, G. G. Silva, N. Quintanal, C. Blanco, R. L. Lavall and R. Santamaria, *J. Phys. Chem. C*, 2020, **124**, 15818–15830.
- 13 M. Forsyth, L. Porcarelli, X. Wang, N. Goujon and D. Mecerreyres, *Acc. Chem. Res.*, 2019, **52**, 686–694.
- 14 S. Bi, H. Banda, M. Chen, L. Niu, M. Chen, T. Wu, J. Wang, R. Wang, J. Feng, T. Chen, M. Dincă, A. A. Kornyshev and G. Feng, *Nat. Mater.*, 2020, **19**, 552–558.
- 15 M. Chen, J. Wu, T. Ye, J. Ye, C. Zhao, S. Bi, J. Yan, B. Mao and G. Feng, *Nat. Commun.*, 2020, **11**, 5809.
- 16 S. Zeng, X. Zhang, L. Bai, X. Zhang, H. Wang, J. Wang, D. Bao, M. Li, X. Liu and S. Zhang, *Chem. Rev.*, 2017, **117**, 9625–9673.
- 17 L. C. Tome and I. M. Marrucho, *Chem. Soc. Rev.*, 2016, **45**, 2785–2824.
- 18 Z. Deng, T. Wan, D. Chen, W. Ying, Y.-J. Zeng, Y. Yan and X. Peng, *Small*, 2020, **16**, 2002699.
- 19 S. Rengshausen, C. Van Stappen, N. Levin, S. Tricard, K. L. Luska, S. DeBeer, B. Chaudret, A. Bordet and W. Leitner, *Small*, 2021, **17**, 2006683.
- 20 P. McNeice, A. Reid, H. T. Imam, C. McDonagh, J. D. Walby, T. J. Collins, A. C. Marr and P. C. Marr, *Environ. Sci. Technol.*, 2020, **54**, 14026–14035.
- 21 R. Hayes, G. G. Warr and R. Atkin, *Chem. Rev.*, 2015, **115**, 6357–6426.
- 22 M. A. Gebbie, A. M. Smith, H. A. Dobbs, A. A. Lee, G. G. Warr, X. Banquy, M. Valtiner, M. W. Rutland, J. N. Israelachvili, S. Perkin and R. Atkin, *Chem. Commun.*, 2017, **53**, 1214–1224.
- 23 Y.-L. Wang, Z.-Y. Lu and A. Laaksonen, *Phys. Chem. Chem. Phys.*, 2014, **16**, 20731–20740.
- 24 Y.-L. Wang, A. Laaksonen and Z.-Y. Lu, *Phys. Chem. Chem. Phys.*, 2013, **15**, 13559–13569.
- 25 M. Dong, K. Zhang, X. Wan, S. Wang, S. Fan, Z. Ye, Y. Wang, Y. Yan and X. Peng, *Small*, 2022, **18**, 2108026.
- 26 J. Comtet, A. Niguès, V. Kaiser, B. Coasne, L. Bocquet and A. Siria, *Nat. Mater.*, 2017, **16**, 634–639.
- 27 M. Sha, G. Wu, Y. Liu, Z. Tang and H. Fang, *J. Phys. Chem. C*, 2009, **113**, 4618–4622.
- 28 R. An, G. Zhou, Y. Zhu, W. Zhu, L. Huang and F. U. Shah, *Adv. Mater. Interfaces*, 2018, **5**, 1800263.
- 29 A. Filippov and O. N. Antzutkin, *Phys. Chem. Chem. Phys.*, 2018, **20**, 6316–6320.
- 30 A. Filippov, N. Azancheev, F. U. Shah, S. Glavatskikh and O. N. Antzutkin, *Microporous Mesoporous Mater.*, 2016, **230**, 128–134.
- 31 C. Pinilla, M. G. Del Pópolo, R. M. Lynden-Bell and J. Kohanoff, *J. Phys. Chem. B*, 2005, **109**, 17922–17927.
- 32 P. K. Cooper, J. Staddon, S. Zhang, Z. M. Aman, R. Atkin and H. Li, *Front. Chem.*, 2019, **7**, 287.
- 33 J. Sweeney, F. Hausen, R. Hayes, G. B. Webber, F. Endres, M. W. Rutland, R. Bennewitz and R. Atkin, *Phys. Rev. Lett.*, 2012, **109**, 155502.
- 34 R. M. Espinosa-Marzal, A. Arcifa, A. Rossi and N. D. Spencer, *J. Phys. Chem. Lett.*, 2014, **5**, 179–184.
- 35 Z. Li, A. Dolocan, O. Morales-Collazo, J. T. Sadowski, H. Celio, R. Chrostowski, J. F. Brennecke and F. Mangolini, *Adv. Mater. Interfaces*, 2020, **7**, 2000426.
- 36 A. Sheehan, L. A. Jurado, S. N. Ramakrishna, A. Arcifa, A. Rossi, N. D. Spencer and R. M. Espinosa-Marzal, *Nanoscale*, 2016, **8**, 4094–4106.
- 37 S. Di Lecce, A. A. Kornyshev, M. Urbakh and F. Bresme, *Phys. Chem. Chem. Phys.*, 2021, **23**, 22174–22183.
- 38 R. Atkin, N. Borisenko, M. Drüscher, S. Z. El Abedin, F. Endres, R. Hayes, B. Huber and B. Roling, *Phys. Chem. Chem. Phys.*, 2011, **13**, 6849–6857.
- 39 K. Shimizu, A. Pensado, P. Malfreyt, A. A. H. Pádua and J. N. Canongia Lopes, *Faraday Discuss.*, 2012, **154**, 155–169.
- 40 R. Hayes, N. Borisenko, M. K. Tam, P. C. Howlett, F. Endres and R. Atkin, *J. Phys. Chem. C*, 2011, **115**, 6855–6863.
- 41 R. Hayes, G. G. Warr and R. Atkin, *Phys. Chem. Chem. Phys.*, 2010, **12**, 1709–1723.
- 42 M. Mezger, H. Schroder, H. Reichert, S. Schramm, J. S. Okasinski, S. Schoder, V. Honkimaki, M. Deutsch, B. M. Ocko, J. Ralston, M. Rohwerder, M. Stratmann and H. Dosch, *Science*, 2008, **322**, 424–428.
- 43 R. Atkin and G. G. Warr, *J. Phys. Chem. C*, 2007, **111**, 5162–5168.
- 44 R. G. Horn, D. F. Evans and B. W. Ninham, *J. Phys. Chem.*, 1988, **92**, 3531–3537.
- 45 F. Buchner, K. Forster-Tonigold, M. Bozorgchenani, A. Gross and R. J. Behm, *J. Phys. Chem. Lett.*, 2016, **7**, 226–233.
- 46 X. Gong, A. Kozbial and L. Li, *Chem. Sci.*, 2015, **6**, 3478–3482.
- 47 X. Wang, M. Salari, D.-E. Jiang, J. Chapman Varela, B. Anasori, D. J. Wesolowski, S. Dai, M. W. Grinstaff and Y. Gogotsi, *Nat. Rev. Mater.*, 2020, **5**, 787–808.
- 48 D. S. Silvester, R. Jamil, S. Doblinger, Y. Zhang, R. Atkin and H. Li, *J. Phys. Chem. C*, 2021, **125**, 13707–13720.
- 49 R. Atkin, N. Borisenko, M. Drüscher, S. Z. El Abedin, F. Endres, R. Hayes, B. Huber and B. Roling, *Phys. Chem. Chem. Phys.*, 2011, **13**, 6849–6857.
- 50 A. M. Smith, K. R. J. Lovelock, N. N. Gosvami, T. Welton and S. Perkin, *Phys. Chem. Chem. Phys.*, 2013, **15**, 15317–15320.
- 51 P. K. Cooper, C. J. Wear, H. Li and R. Atkin, *ACS Sustainable Chem. Eng.*, 2017, **5**, 11737–11743.
- 52 R. An, X. Qiu, F. U. Shah, K. Riehemann and H. Fuchs, *Phys. Chem. Chem. Phys.*, 2020, **22**, 14941–14952.
- 53 H. Li, M. W. Rutland and R. Atkin, *Phys. Chem. Chem. Phys.*, 2013, **15**, 14616–14623.
- 54 H. Li, M. W. Rutland, M. Watanabe and R. Atkin, *Faraday Discuss.*, 2017, **199**, 311–322.
- 55 R. Futamura, T. Iiyama, Y. Takasaki, Y. Gogotsi, M. J. Biggs, M. Salanne, J. Ségalini, P. Simon and K. Kaneko, *Nat. Mater.*, 2017, **16**, 1225–1232.
- 56 M. V. Fedorov and A. A. Kornyshev, *Chem. Rev.*, 2014, **114**, 2978–3036.

- 57 Y. Zhou and J. Qu, *ACS Appl. Mater. Interfaces*, 2017, **9**, 3209–3222.
- 58 Y.-L. Wang, B. Li, S. Sarman, F. Mocci, Z.-Y. Lu, J. Yuan, A. Laaksonen and M. D. Fayer, *Chem. Rev.*, 2020, **120**, 5798–5877.
- 59 G. Binnig, C. F. Quate and C. Gerber, *Phys. Rev. Lett.*, 1986, **56**, 930–933.
- 60 C. Gerber and H. P. Lang, *Nat. Nanotechnol.*, 2006, **1**, 3–5.
- 61 D. Alsteens, H. E. Gaub, R. Newton, M. Pfreundschuh, C. Gerber and D. J. Müller, *Nat. Rev. Mater.*, 2017, **2**, 17008.
- 62 M. Krieg, G. Fläschner, D. Alsteens, B. M. Gaub, W. H. Roos, G. J. L. Wuite, H. E. Gaub, C. Gerber, Y. F. Dufrêne and D. J. Müller, *Nat. Rev. Phys.*, 2019, **1**, 41–57.
- 63 N. Pavliček and L. Gross, *Nat. Rev. Chem.*, 2017, **1**, 0005.
- 64 B. Bhushan, *Handbook of Micro/Nano Tribology*, CRC Press, Boca Raton, 1999.
- 65 R. García and R. Pérez, *Surf. Sci. Rep.*, 2002, **47**, 197–301.
- 66 H.-J. Butt, B. Cappella and M. Kappl, *Surf. Sci. Rep.*, 2005, **59**, 1–152.
- 67 X. Zhang, Y.-X. Zhong, J.-W. Yan, Y.-Z. Su, M. Zhang and B.-W. Mao, *Chem. Commun.*, 2012, **48**, 582–584.
- 68 H. Li, Y. Zhang, S. Jones, R. Segalman, G. G. Warr and R. Atkin, *J. Colloid Interface Sci.*, 2022, **606**, 1170–1178.
- 69 B. Bhushan and Y. C. Jung, *Prog. Mater. Sci.*, 2011, **56**, 1–108.
- 70 M. B. Salerno, X. Li and B. E. Logan, *Colloids Surf., B*, 2007, **59**, 46–51.
- 71 T. Das, T. Becker and B. N. Nair, *Thin Solid Films*, 2010, **518**, 2769–2774.
- 72 V. Vadillo-Rodrigues, H. J. Busscher, W. Norde, J. De Vries, R. J. B. Dijkstra, I. Stokroos and H. C. van der Mei, *Appl. Environ. Microbiol.*, 2004, **70**, 5441–5446.
- 73 B. Bhushan, K. J. Kwak and M. Palacio, *J. Phys.: Condens. Matter*, 2008, **20**, 1–34.
- 74 B. Bhushan, *Wear*, 2005, **259**, 1507–1531.
- 75 B. Bhushan, *Beilstein J. Nanotechnol.*, 2011, **2**, 66–84.
- 76 P. Lazar, S. Zhang, K. Šafářová, Q. Li, J. P. Froning, J. Granatier, P. Hobza, R. Zbořil, F. Besenbacher, M. Dong and M. Otyepka, *ACS Nano*, 2013, **7**, 1646–1651.
- 77 L. Xiang, J. Zhang, L. Gong and H. Zeng, *Soft Matter*, 2020, **16**, 6697–6719.
- 78 M. Radiom, *Curr. Opin. Colloid Interface Sci.*, 2019, **39**, 148–161.
- 79 D. Leckband and J. Israelachvili, *Q. Rev. Biophys.*, 2001, **34**, 105–267.
- 80 R. H. French, *J. Am. Ceram. Soc.*, 2000, **83**, 2117–2146.
- 81 J. D. van der Waals, *The Thermodynamic Theory of Capillarity Under the Hypothesis of a Continuous Variation of Density*, Verhandel. Konink. Akad. Weten. Amsterdam, The Netherlands, 1893.
- 82 F. L. Leite, C. C. Bueno, A. L. Da Róz, E. C. Ziernath and O. N. Oliveira, *Int. J. Mol. Sci.*, 2012, **13**, 12773–12856.
- 83 D. Tabor and R. H. S. Winterton, *Proc. R. Soc. London, Ser. A*, 1969, **312**, 435–450.
- 84 N. Hjalmarsson, R. Atkin and M. W. Rutland, *Chem. Commun.*, 2017, **53**, 647–650.
- 85 C. Rodenbücher, K. Wippermann and C. Korte, *Appl. Sci.*, 2019, **9**, 2207.
- 86 L. A. Jurado, H. Kim, A. Rossi, A. Arcifa, J. K. Schuh, N. D. Spencer, C. Leal, R. H. Ewoldt and R. M. Espinosa-Marzal, *Phys. Chem. Chem. Phys.*, 2016, **18**, 22719–22730.
- 87 Z. Wang, H. Li, R. Atkin and C. Priest, *Langmuir*, 2016, **32**, 8818–8825.
- 88 A. M. Smith, A. A. Lee and S. Perkin, *J. Phys. Chem. Lett.*, 2016, **7**, 2157–2163.
- 89 H.-W. Cheng, P. Stock, B. Moeremans, T. Baimpos, X. Banquy, F. U. Renner and M. Valtiner, *Adv. Mater. Interfaces*, 2015, **2**, 1500159.
- 90 M. A. Gebbie, H. A. Dobbs, M. Valtiner and J. N. Israelachvili, *Proc. Natl. Acad. Sci. U. S. A.*, 2015, **112**, 7432–7437.
- 91 M. A. Gebbie, M. Valtiner, X. Banquy, E. T. Fox, W. A. Henderson and J. N. Israelachvili, *Proc. Natl. Acad. Sci. U. S. A.*, 2013, **110**, 9674–9679.
- 92 E. Meyer, *Prog. Surf. Sci.*, 1992, **41**, 3–49.
- 93 M. J. Wydro, G. G. Warr and R. Atkin, *Langmuir*, 2015, **31**, 5513–5520.
- 94 K.-I. Amano, Y. Yokota, T. Ichii, N. Yoshida, N. Nishi, S. Katakura, A. Imanishi, K.-I. Fukui and T. Sakka, *Phys. Chem. Chem. Phys.*, 2017, **19**, 30504–30512.
- 95 C. M. Mate, *Tribology on the Small Scale: A Bottom Up Approach to Friction, Lubrication, and Wear*, Oxford University Press, Oxford, New York, 2008.
- 96 G. Amontons, *Mem. l'Academie R. A.*, 1699, 257–282.
- 97 C. A. Coulomb, *Mem. Math. Phys. Paris X*, 1785, 161–342.
- 98 B. Quignon, G. A. Pilkington, E. Thormann, P. M. Claesson, M. N. R. Ashfold, D. Mattia, H. Leese, S. A. Davis and W. H. Briscoe, *ACS Nano*, 2013, **7**, 10850–10862.
- 99 J. P. Gao, W. D. Luedtke, D. Gourdon, M. Ruths, J. N. Israelachvili and U. Landman, *J. Phys. Chem. B*, 2004, **108**, 3410–3425.
- 100 J. B. Pethica and W. C. Oliver, *Phys. Scr.*, 1987, **T19**, 61–66.
- 101 P. K. Cooper, H. Li, M. W. Rutland, G. B. Webber and R. Atkin, *Phys. Chem. Chem. Phys.*, 2016, **18**, 23657–23662.
- 102 N. Hjalmarsson, R. Atkin and M. W. Rutland, *Phys. Chem. Chem. Phys.*, 2016, **18**, 9232–9239.
- 103 H. Li, T. Niemann, R. Ludwig and R. Atkin, *J. Phys. Chem. Lett.*, 2020, **11**, 3905–3910.
- 104 T. Niemann, H. Li, G. G. Warr, R. Ludwig and R. Atkin, *J. Phys. Chem. Lett.*, 2019, **10**, 7368–7373.
- 105 G. A. Pilkington, R. Welbourn, A. Oleshkeyevych, S. Watanabe, P. Pedraz, M. Radiom, S. Glavatskih and M. W. Rutland, *Phys. Chem. Chem. Phys.*, 2020, **22**, 28191–28201.
- 106 Z. Deng, A. Smolyanitsky, Q. Li, X.-Q. Feng and R. J. Cannara, *Nat. Mater.*, 2012, **11**, 1032–1037.
- 107 Z. Deng, N. N. Klimov, S. D. Solares, T. Li, H. Xu and R. J. Cannara, *Langmuir*, 2013, **29**, 235–243.
- 108 Z. Ye and A. Martini, *Langmuir*, 2014, **30**, 14707–14711.

- 109 M. Tripathi, F. Awaja, G. Paolicelli, R. Bartali, E. Iacob, S. Valeri, S. Ryu, S. Signetti, G. Speranza and N. M. Pugno, *Nanoscale*, 2016, **8**, 6646–6658.
- 110 E. Thormann, *Nat. Mater.*, 2013, **12**, 468.
- 111 A. Smolyanitsky and J. P. Killgore, *Phys. Rev. B: Condens. Matter Mater. Phys.*, 2012, **86**, 125432.
- 112 A. Smolyanitsky, S. Zhu, Z. Deng, T. Li and R. J. Cannara, *RSC Adv.*, 2014, **4**, 26721–26728.
- 113 W. Ouyang, S. N. Ramakrishna, A. Rossi, M. Urbakh, N. D. Spencer and A. Arcifa, *Phys. Rev. Lett.*, 2019, **123**, 116102.
- 114 E. Meyer, T. Gyalog, R. M. Overney and K. Dransfeld, *Nanoscience: Friction and Rheology on the Nanometer Scale*, World Scientific, Singapore, 1998.
- 115 J. Klein and E. Kumacheva, *J. Chem. Phys.*, 1998, **108**, 6996–7009.
- 116 E. Kumacheva and J. Klein, *J. Chem. Phys.*, 1998, **108**, 7010–7022.
- 117 R. An, L. Huang, Y. Long, B. Kalanyan, X. Lu and K. E. Gubbins, *Langmuir*, 2016, **32**, 743–750.
- 118 C. L. M. H. Navier, *Mem Acad. Sci. Inst. France*, 1823, **1**, 414–416.
- 119 L. Bocquet and E. Charlaix, *Chem. Soc. Rev.*, 2010, **39**, 1073–1095.
- 120 J. S. Ellis and M. Thompson, *Phys. Chem. Chem. Phys.*, 2004, **6**, 4928–4938.
- 121 Y. Li, Y. Pan and X. Zhao, *Appl. Sci.*, 2018, **8**, 931.
- 122 A. Maali and B. Bhushan, *J. Phys.: Condens. Matter*, 2008, **20**, 315201.
- 123 D. Y. C. Chan and R. G. Horn, *J. Chem. Phys.*, 1985, **83**, 5311–5324.
- 124 O. I. Vinogradova, *Langmuir*, 1995, **11**, 2213–2220.
- 125 J. Sweeney, G. B. Webber and R. Atkin, *Phys. Chem. Chem. Phys.*, 2015, **17**, 26629–26637.
- 126 P. C. Nalam, A. Sheehan, M. Han and R. M. Espinosa-Marzal, *Adv. Mater. Interfaces*, 2020, **7**, 2000314.
- 127 P. G. de Gennes, *Langmuir*, 2002, **18**, 3413–3414.
- 128 D. C. Tretheway and C. D. Meinhart, *Phys. Fluids*, 2002, **14**, L9–L12.
- 129 N. Voeltzel, A. Giuliani, N. Fillot, P. Vergne and L. Joly, *Phys. Chem. Chem. Phys.*, 2015, **17**, 23226–23235.
- 130 R. Lhermerout and S. Perkin, *Phys. Rev. Fluids*, 2018, **3**, 014201.
- 131 N. Voeltzel, N. Fillot, P. Vergne and L. Joly, *J. Phys. Chem. C*, 2018, **122**, 2145–2154.
- 132 J. M. Black, D. Walters, A. Labuda, G. Feng, P. C. Hillesheim, S. Dai, P. T. Cummings, S. V. Kalinin, R. Proksch and N. Balke, *Nano Lett.*, 2013, **13**, 5954–5960.
- 133 T. Cui, A. Lahiri, T. Carstens, N. Borisenko, G. Pulletikurthi, C. Kuhl and F. Endres, *J. Phys. Chem. C*, 2016, **120**, 9341–9349.
- 134 L. A. Jurado and R. M. Espinosa-Marzal, *Sci. Rep.*, 2017, **7**, 4225.
- 135 H. Li, F. Endres and R. Atkin, *Phys. Chem. Chem. Phys.*, 2013, **15**, 14624–14633.
- 136 H. Li, R. J. Wood, F. Endres and R. Atkin, *J. Phys.: Condens. Matter*, 2014, **26**, 284115.
- 137 O. Y. Fajardo, F. Bresme, A. A. Kornyshev and M. Urbakh, *Sci. Rep.*, 2015, **5**, 7698.
- 138 A. Elbourne, K. Voitchovsky, G. G. Warr and R. Atkin, *Chem. Sci.*, 2015, **6**, 527–536.
- 139 D. Wakeham, R. Hayes, G. G. Warr and R. Atkin, *J. Phys. Chem. B*, 2009, **113**, 5961–5966.
- 140 A. Cook, K. Ueno, M. Watanabe, R. Atkin and H. Li, *J. Phys. Chem. C*, 2017, **121**, 15728–15734.
- 141 M. Radiom, P. Pedraz, G. Pilkington, P. Rohlmann, S. Glavatskikh and M. W. Rutland, *Colloids Interfaces*, 2018, **2**, 60.
- 142 J. Hoth, F. Hausen, M. H. Müser and R. Bennewitz, *J. Phys.: Condens. Matter*, 2014, **26**, 284110.
- 143 Y. Wang, C. Wang, Y. Zhang, F. Huo, H. He and S. Zhang, *Small*, 2019, **15**, 1804508.
- 144 J. J. Nainaparampil, K. C. Eapen, J. H. Sanders and A. A. Voevodin, *J. Microelectromech. Syst.*, 2007, **16**, 836–843.
- 145 I. Minami, *Molecules*, 2009, **14**, 2286–2305.
- 146 S. Di Lecce, A. A. Kornyshev, M. Urbakh and F. Bresme, *ACS Appl. Mater. Interfaces*, 2020, **12**, 4105–4113.
- 147 R. M. Espinosa-Marzal, A. Arcifa, A. Rossi and N. D. Spencer, *J. Phys. Chem. C*, 2014, **118**, 6491–6503.
- 148 B. Wang and L. Li, *Nanoscale*, 2021, **13**, 17961–17971.
- 149 C. S. Perez-Martinez and S. Perkin, *Langmuir*, 2019, **35**, 15444–15450.
- 150 S. Di Lecce, A. A. Kornyshev, M. Urbakh and F. Bresme, *ACS Nano*, 2020, **14**, 13256–13267.
- 151 S. Bovio, A. Podestà, C. Lenardi and P. Milani, *J. Phys. Chem. B*, 2009, **113**, 6600–6603.
- 152 X. Gong, A. Kozbial, F. Rose and L. Li, *ACS Appl. Mater. Interfaces*, 2015, **7**, 7078–7081.
- 153 A. Deyko, T. Cremer, F. Rietzler, S. Perkin, L. Crowhurst, T. Welton, H.-P. Steinrück and F. Maier, *J. Phys. Chem. C*, 2013, **117**, 5101–5111.
- 154 L. J. D. Frink and F. V. Swol, *J. Chem. Phys.*, 1998, **108**, 5588–5598.
- 155 R. G. Horn and J. N. Israelachvili, *J. Chem. Phys.*, 1981, **75**, 1400–1411.
- 156 R. Á. Asencio, E. D. Cranston, R. Atkin and M. W. Rutland, *Langmuir*, 2012, **28**, 9967–9976.
- 157 A. David, O. Y. Fajardo, A. A. Kornyshev, M. Urbakh and F. Bresme, *Faraday Discuss.*, 2017, **199**, 279–297.
- 158 A. C. F. Mendonça, A. A. H. Pádua and P. Malfreyt, *J. Chem. Theory Comput.*, 2013, **9**, 1600–1610.
- 159 A. Martini, H.-Y. Hsu, N. A. Patankar and S. Lichten, *Phys. Rev. Lett.*, 2008, **100**, 206001.
- 160 J. Comtet, A. Niguès, V. Kaiser, B. Coasne, L. Bocquet and A. Siria, *Nat. Mater.*, 2017, **16**, 634–639.
- 161 B. Wang and L. Li, *Langmuir*, 2021, **37**, 14753–14759.
- 162 J. Liu, J. Li, B. Yu, B. Ma, Y. Zhu, X. Song, X. Cao, W. Yang and F. Zhou, *Langmuir*, 2011, **27**, 11324–11331.
- 163 Y. Wang, F. Huo, H. He and S. Zhang, *Phys. Chem. Chem. Phys.*, 2018, **20**, 17773–17780.
- 164 L. T. W. Lim, A. T. S. Wee and S. J. O'Shea, *J. Chem. Phys.*, 2009, **130**, 134703.

- 165 H. G. Ozcelik and M. Barisik, *Phys. Chem. Chem. Phys.*, 2019, **21**, 7576–7587.
- 166 C. Merlet, B. Rotenberg, P. A. Madden and M. Salanne, *Phys. Chem. Chem. Phys.*, 2013, **15**, 15781–15792.
- 167 S. Ntim and M. Sulpizi, *Phys. Chem. Chem. Phys.*, 2020, **22**, 10786–10791.
- 168 A. Lewandowski, A. Olejniczak, M. Galinski and I. Stepniaak, *J. Power Sources*, 2010, **195**, 5814–5819.
- 169 A. Elbourne, S. McDonald, K. Voichovsky, F. Endres, G. G. Warr and R. Atkin, *ACS Nano*, 2015, **9**, 7608–7620.
- 170 Y.-L. Wang and A. Laaksonen, *Phys. Chem. Chem. Phys.*, 2014, **16**, 23329–23339.
- 171 R. An, Y. Wei, X. Qiu, Z. Dai, M. Wu, E. Gnecco, F. U. Shah and W. Zhang, *Friction*, 2022, DOI: [10.1007/s40544-021-0566-5](https://doi.org/10.1007/s40544-021-0566-5).
- 172 I. Bou-Malham and L. Bureau, *Soft Matter*, 2010, **6**, 4062–4065.
- 173 P. S. Gil, S. J. Jorgenson, A. R. Riet and D. J. Lacks, *J. Phys. Chem. C*, 2018, **122**, 27462–27468.
- 174 V. Hoffmann, G. Pulletikurthi, T. Carstens, A. Lahiri, A. Borodin, M. Schammer, B. Horstmann, A. Latz and F. Endres, *Phys. Chem. Chem. Phys.*, 2018, **20**, 4760–4771.
- 175 R. Atkin, S. Z. El Abedin, R. Hayes, L. H. S. Gasparotto, N. Borisenko and F. Endres, *J. Phys. Chem. C*, 2009, **113**, 13266–13272.
- 176 H. Li, R. J. Wood, M. W. Rutland and R. Atkin, *Chem. Commun.*, 2014, **50**, 4368–4370.
- 177 F. Hausen, N. N. Gosvami and R. Bennewitz, *Electrochim. Acta*, 2011, **56**, 10694–10700.
- 178 A. Labuda, F. Hausen, N. N. Gosvami, P. H. Grütter, R. B. Lennox and R. Bennewitz, *Langmuir*, 2011, **27**, 2561–2566.
- 179 S. Perkin, T. Albrecht and J. Klein, *Phys. Chem. Chem. Phys.*, 2010, **12**, 1243–1247.
- 180 G. Kraemer and R. Bennewitz, *J. Phys. Chem. C*, 2019, **123**, 28284–28290.
- 181 J. M. Black, M. Zhu, P. Zhang, R. R. Unocic, D. Guo, M. B. Okatan, S. Dai, P. T. Cummings, S. V. Kalinin, G. Feng and N. Balke, *Sci. Rep.*, 2016, **6**, 32389.
- 182 H. W. Cheng, J. N. Dienemann, P. Stock, C. Merola, Y. J. Chen and M. Valtiner, *Sci. Rep.*, 2016, **6**, 30058.
- 183 D. A. Rakov, F. Chen, S. A. Ferdousi, H. Li, T. Pathirana, A. N. Simonov, P. C. Howlett, R. Atkin and M. Forsyth, *Nat. Mater.*, 2020, **19**, 1096.
- 184 S. Bi, R. Wang, S. Liu, J. Yan, B. Mao, A. A. Kornyshev and G. Feng, *Nat. Commun.*, 2018, **9**, 5222.
- 185 O. Y. Fajardo, F. Bresme, A. A. Kornyshev and M. Urbakh, *ACS Nano*, 2017, **11**, 6825–6831.
- 186 A. Broderick and J. T. Newberg, Water at Ionic Liquid Interfaces, in *Ionic Liquids: Current State and Future Directions*, ed. M. B. Shiflett and A. M. Scurto, ACS Symposium Series, 2017, vol. 1250, pp. 227–249.
- 187 S. Liu, M. Li, J. Peng, L. Chen, B. Mao and J. Yan, *Chem. Commun.*, 2020, **56**, 15064–15067.
- 188 Y. Zhong, J. Yan, M. Li, L. Chen and B. Mao, *ChemElectroChem*, 2016, **3**, 2221–2226.
- 189 O. Werzer, E. D. Cranston, G. G. Warr, R. Atkin and M. W. Rutland, *Phys. Chem. Chem. Phys.*, 2012, **14**, 5147–5152.
- 190 M. Han and R. M. Espinosa-Marzal, *Lubricants*, 2018, **6**, 64.
- 191 T. Shoaib, J. Heintz, J. A. Lopez-Berganza, R. Muro-Barrios, S. A. Egner and R. M. Espinosa-Marzal, *Langmuir*, 2018, **34**, 756–765.
- 192 M. Jitvisate and J. R. T. Seddon, *J. Phys. Chem. C*, 2017, **121**, 18593–18597.
- 193 J. A. Smith, O. Werzer, G. B. Webber, G. G. Warr and R. Atkin, *J. Phys. Chem. Lett.*, 2010, **1**, 64–68.
- 194 X. Qiu, L. Lu, Z. Qu, J. Liao, Q. Fan, F. U. Shah, W. Zhang and R. An, *Friction*, 2022, **10**, 268–281.
- 195 H. Li, A. E. Somers, P. C. Howlett, M. W. Rutland, M. Forsyth and R. Atkin, *Phys. Chem. Chem. Phys.*, 2016, **18**, 6541–6547.
- 196 M. Fan, D. Yang, X. Wang, W. Liu and H. Fu, *Ind. Eng. Chem. Res.*, 2014, **53**, 17952–17960.
- 197 V. Pejaković, C. Tomastik, N. Dörr and M. Kalin, *Tribol. Int.*, 2016, **97**, 234–243.
- 198 D. Jiang, L. Hu and D. Feng, *Publ. Sci.*, 2013, **25**, 195–207.
- 199 J. S. Keist, J. A. Hammons, P. K. Wright, J. W. Evans and C. A. Orme, *Electrochim. Acta*, 2020, **342**, 136073.
- 200 T. Fukuma and R. Garcia, *ACS Nano*, 2018, **12**, 11785–11797.
- 201 H. Söngen, B. Reischl, K. Miyata, R. Bechstein, P. Raiteri, A. L. Rohl, J. D. Gale, T. Fukuma and A. Kühnle, *Phys. Rev. Lett.*, 2018, **120**, 116101.
- 202 Z. Li, Q. Liu, D. Zhang, Y. Wang, Y. Zhang, Q. Li and M. Dong, *Nanoscale Horiz.*, 2022, **7**, 368–375.
- 203 S. Zhou, K. S. Panse, M. H. Motavaselian, N. R. Aluru and Y. Zhang, *ACS Nano*, 2020, **14**, 17515–17523.
- 204 W. Zhou, S. Inoue, T. Iwashashi, K. Kanai, K. Seki, T. Miyamae, D. Kim, Y. Katayama and Y. Ouchi, *Electrochim. Commun.*, 2010, **12**, 672–675.
- 205 K. Motobayashi, K. Minami, N. Nishi, T. Sakka and M. Osawa, *J. Phys. Chem. Lett.*, 2013, **4**, 3110–3114.
- 206 G. Pulletikurthi, M. Shapouri Ghazvini, T. Cui, N. Borisenko, T. Carstens, A. Borodin and F. Endres, *Dalton Trans.*, 2017, **46**, 455–464.
- 207 D. Bedrov, J.-P. Piquemal, O. Borodin, A. D. MacKerell, B. Roux and C. Schröder, *Chem. Rev.*, 2019, **119**, 7940–7995.
- 208 A. Moradzadeh, M. H. Motavaselian, S. Y. Mashayak and N. R. Aluru, *J. Chem. Theory Comput.*, 2018, **14**, 3252–3261.
- 209 F. Uhlig, J. Zeman, J. Smiatek and C. Holm, *J. Chem. Theory Comput.*, 2018, **14**, 1471–1486.
- 210 F. L. Leite and P. S. P. Herrmann, *J. Adhes. Sci. Technol.*, 2005, **19**, 365–405.
- 211 R. García, *Amplitude Modulation Atomic Force Microscopy*, Wiley-VCH Verlag GmbH & Co. KGaA, Weinheim, Germany, 2010.
- 212 Y. Wei, Z. Dai, Y. Dong, A. Filippov, X. Ji, A. Laaksonen, F. U. Shah, R. An and H. Fuchs, *Phys. Chem. Chem. Phys.*, 2022, **24**, 12808–12815.
- 213 Y. Wei, Y. Dong, X. Ji, F. Ullah Shah, A. Laaksonen, R. An and K. Riehemann, *J. Mol. Liq.*, 2022, **350**, 118506.